

Conserved class B GPCR activation by a biased intracellular agonist

<https://doi.org/10.1038/s41586-023-06467-w>

Received: 27 February 2023

Accepted: 20 July 2023

Published online: 31 July 2023

 Check for updates

Li-Hua Zhao^{1,2,3}✉, Qian He^{1,2,3}, Qingning Yuan^{1,3}, Yimin Gu^{1,2}, Xinheng He^{1,2}, Hong Shan¹, Junrui Li¹, Kai Wang¹, Yang Li^{1,2}, Wen Hu¹, Kai Wu¹, Jianhua Shen^{1,2} & H. Eric Xu^{1,2}✉

Class B G-protein-coupled receptors (GPCRs), including glucagon-like peptide 1 receptor (GLP1R) and parathyroid hormone 1 receptor (PTH1R), are important drug targets^{1–5}. Injectable peptide drugs targeting these receptors have been developed, but orally available small-molecule drugs remain under development^{6,7}. Here we report the high-resolution structure of human PTH1R in complex with the stimulatory G protein (G_s) and a small-molecule agonist, PCO371, which reveals an unexpected binding mode of PCO371 at the cytoplasmic interface of PTH1R with G_s . The PCO371-binding site is totally different from all binding sites previously reported for small molecules or peptide ligands in GPCRs. The residues that make up the PCO371-binding pocket are conserved in class B GPCRs, and a single alteration in PTH2R and two residue alterations in GLP1R convert these receptors to respond to PCO371. Functional assays reveal that PCO371 is a G-protein-biased agonist that is defective in promoting PTH1R-mediated arrestin signalling. Together, these results uncover a distinct binding site for designing small-molecule agonists for PTH1R and possibly other members of the class B GPCRs and define a receptor conformation that is specific only for G-protein activation but not arrestin signalling. These insights should facilitate the design of distinct types of class B GPCR small-molecule agonist for various therapeutic indications.

Class B GPCRs are peptide hormone receptors that are drug targets for many diseases, including osteoporosis, type 2 diabetes, obesity, bone metabolism diseases, cardiovascular disease, migraine and depression^{1–4}. Structures of all 15 class B GPCRs with peptide agonists have been determined in recent years², providing important molecular mechanisms of hormone recognition and receptor activation for the whole family of class B GPCRs and rational templates for designing better peptidic and small-molecule drugs². Class B GPCRs are different from class A GPCRs because many therapeutic small-molecule agonist drugs have been developed for class A but not for class B GPCRs⁵. For class B GPCRs, despite great efforts towards discovering orally available non-peptidic agonists, few small-molecule agonists of class B GPCRs are known^{6,7}. This is a difficult problem in class B GPCRs, because their natural ligands are peptide hormones, which activate the receptor through peptide binding to a large open pocket within the receptor transmembrane domain (TMD) and the high-affinity binding of peptide hormones requires the interaction with the receptor extracellular domain (ECD)⁸. So far, only a few small-molecule agonists of GLP1R and PTH1R have been reported^{9–17}. Several structures of GLP1R with a partial or full non-peptidic small-molecule agonist have also been reported^{9,13,18–20}, which reveal that they bind to the same binding site of peptide hormones or to an allosteric site at the cytoplasmic end of TM6 (refs. 9,11,13,18,21). Nonetheless, there are no orally available small-molecule drugs for class B GPCRs. It is challenging but remains a long-term goal to replace the injectable peptide drugs with oral

drugs, with aims to improve the quality of life of patients, the profiles of side-effects and the costs of peptide drugs.

PTH1R is a classic member of the class B GPCRs that regulates calcium homeostasis and skeleton development through activation by two endogenous peptide hormones, parathyroid hormone (PTH) and PTH-related peptide (PTHRP)^{8,22,23}. PTH1R is a clinically proven target for hypoparathyroidism and osteoporosis, which can be treated with injections of PTH or PTHRP analogues^{8,17}. Recently, PCO371 was reported as a potent and orally available small-molecule PTH1R agonist²⁴ that is being evaluated at present in a phase 1 clinical study for the treatment of hypoparathyroidism^{17,25}. However, the molecular mechanism of PTH1R activation by PCO371 remains unknown. In this paper, we report the structure of PTH1R bound to PCO371 and its functional characterization as a G-protein-biased agonist relative to PTH²⁶. The structure reveals that PCO371 binds to an unexpected site at the interface between PTH1R and the G protein, distinct from all other sites known for GPCR ligands. The PCO371-binding pocket is conserved in most class B GPCRs, thus opening a new avenue for designing small-drug molecules targeting specifically to this pocket.

Characterization of PCO371

PCO371 was characterized as an agonist of PTH1R as it can induce the same level of cAMP production as PTH(1–34)¹⁷, but it remains unknown whether PCO371 could induce PTH1R-mediated β-arrestin signalling.

¹State Key Laboratory of Drug Research, Center for Structure and Function of Drug Targets, Shanghai Institute of Materia Medica, Chinese Academy of Sciences, Shanghai, China. ²University of Chinese Academy of Sciences, Beijing, China. ³These authors contributed equally: Li-Hua Zhao, Qian He, Qingning Yuan. ✉e-mail: zhaoliuhawendy@simm.ac.cn; eric.xu@simm.ac.cn

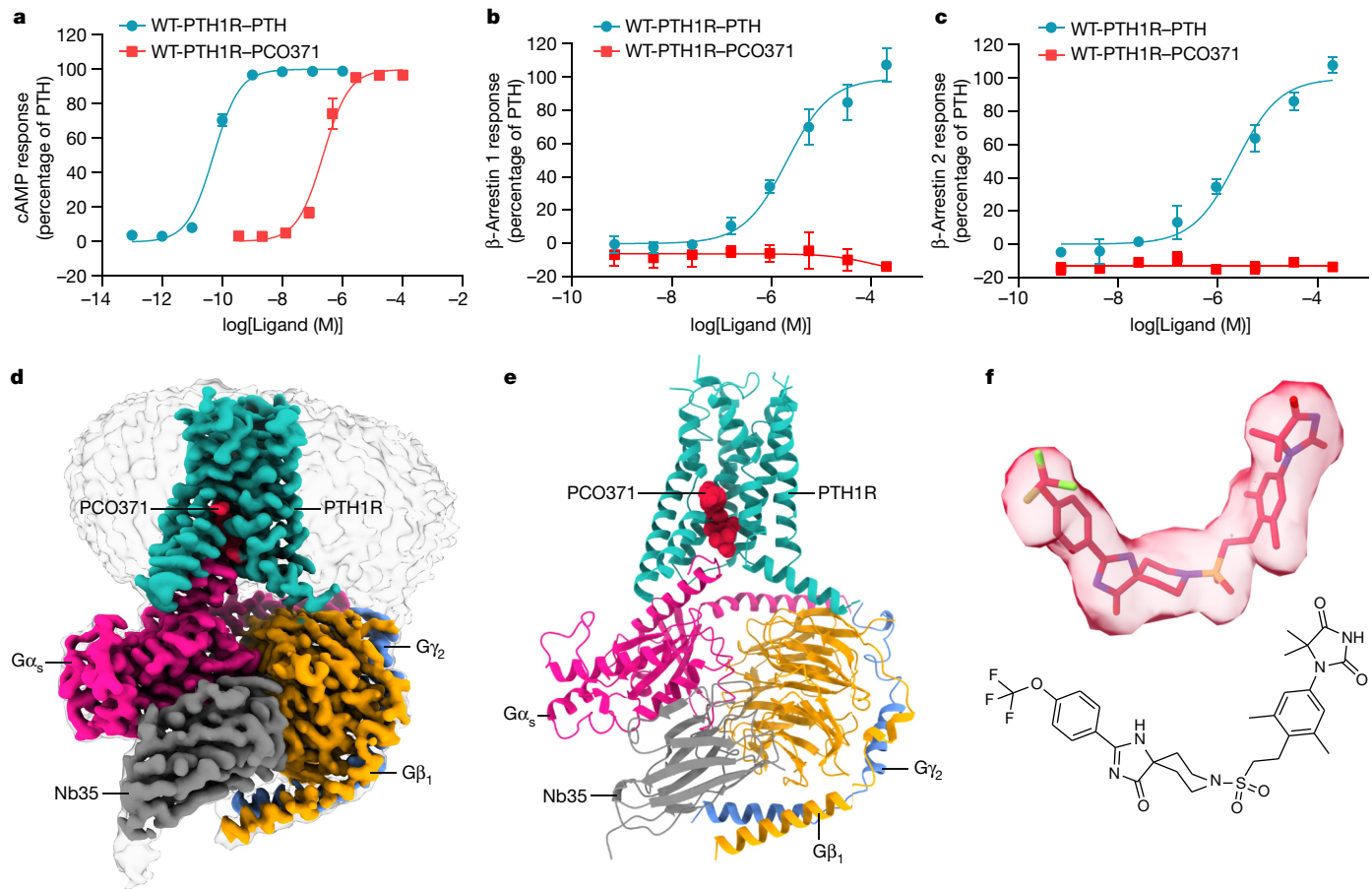


Fig. 1 | Human PTH1R signalling by PCO371 and cryo-EM structure of PTH1R-G_s signalling complex. **a–c**, PCO371 induced PTH1R signalling. Dose-response curves for the cAMP accumulation assay (**a**) and for recruitment assays of β-arrestin 1 (**b**) and β-arrestin 2 (**c**) as induced by PCO371 with PTH as the reference ligand. Data represent means \pm s.e.m. of three independent

experiments ($n=3$), and each experiment was carried out in triplicate. The data were normalized according to the maximal response of PTH. **d**, Cryo-EM map of the PCO371-PTH1R-G_s complex. **e**, Cryo-EM structure model of the PCO371-PTH1R-G_s complex. **f**, Map (top) and chemical structure (bottom) of PCO371.

We first investigated their effects on G-protein signalling pathways using cAMP accumulation (Fig. 1a). We also measured agonist-induced β-arrestin recruitment at PTH1R with two different assays: arrestin recruitment by NanoBiT assays²⁷ and receptor-induced arrestin membrane association by confocal microscopy²⁸ (Fig. 1b,c and Extended Data Fig. 1). We confirmed that PCO371 is a full G-protein agonist, but discovered that PCO371, unlike PTH peptide, is defective in promoting PTH1R-mediated arrestin signalling (Fig. 1a–c). These data suggest that PCO371 is a G-protein-biased agonist with PTH as the reference ligand²⁶.

Structure determination

To study the G-protein-biased agonism of PCO371, we prepared the PCO371-bound PTH1R-G_s complex using the NanoBiT tethering strategy^{29,30} (Methods). The carboxy terminus of PTH1R was truncated to residue H502 to increase the expression level of PTH1R as we showed previously³¹ (Extended Data Fig. 2a). The complex was purified by size-exclusion chromatography and verified by SDS gel electrophoresis (Extended Data Fig. 2b). The structure of the PCO371-PTH1R-G_s complex was solved by cryogenic electron microscopy (cryo-EM) to a high resolution of 2.57 Å (Fig. 1d, Extended Data Fig. 3 and Extended Data Table 1). The high-resolution cryo-EM map is sufficiently clear to place the receptor, the G_s heterotrimer and the small-molecule agonist in the PTH1R-G_s protein complex (Fig. 1d–f and Extended Data Fig. 4). Unlike the peptide-bound PTH1R-G_s structures, the PTH1R ECD was

invisible in this PCO371-bound PTH1R-G_s structure owing to the flexibility of the ECD in the absence of the peptide binding.

Overall architecture

The overall structure of PTH1R exhibits a canonical seven-TMD fold of GPCRs and the hallmark of class B GPCR activation with a kink in the middle of TM6, which is very different from the inactive state of PTH1R³² (Extended Data Fig. 5). We also observed several distinct features in the PCO371-PTH1R-G_s structure compared to three cryo-EM structures of PTH1R in complexes with PTH, PTHRP and long-acting PTH (LA-PTH) reported previously^{23,31,33–35} (Extended Data Figs. 5 and 6a–d). The most notable difference is that PCO371 occupies a distinct ligand-binding pocket of PTH1R, comprising the intracellular portion of TM2, TM3, TM6 and TM7 as well as helix H8, at the interface between PTH1R and the G protein (Extended Data Fig. 5a,b). This binding pocket is different from the peptide-hormone-binding pockets of class B GPCRs and the small-molecule-binding pockets of GLP1R (Fig. 2 and Extended Data Figs. 5b and 6e–l). In responding to PCO371 binding, the extracellular tips of helices TM1, TM6 and TM7 in the PCO371-PTH1R-G_s structure shift anticlockwise by as much as 5–7.5 Å, relative to their positions in the PTH-PTH1R-G_s structure (Extended Data Fig. 5c), which results in a collision between the extracellular end of TM6 and the bound PTH peptide, consistent with the report that the presence of PCO371 would inhibit the binding of PTH to its TMD¹⁷. By contrast, relative to the peptide-bound active PTH1R structures, we observed an approximately

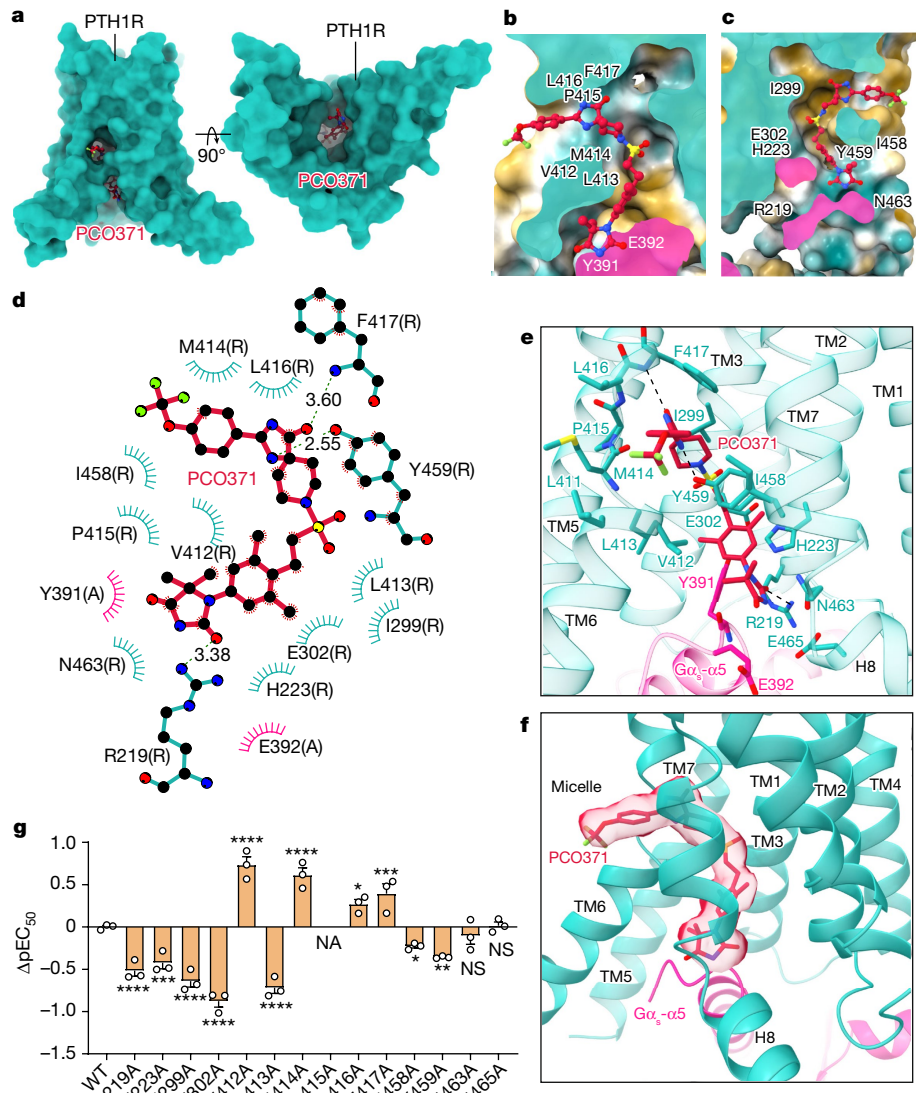


Fig. 2 | Interactions of PCO371 with PTH1R. **a**, Side (left) and intracellular (right) views of the PCO371-binding pocket of PTH1R. **b,c**, Cross-section of the PCO371-binding pocket in PTH1R. **d**, Interacting residues predicted by LigPlot using the full-length model. The single letters in brackets represent the chains in the model. R signifies the receptor (PTH1R), while A signifies G α_s . **e**, Detailed interactions of PCO371 with residues in the binding pocket. **f**, The bound PCO371 at the interface between PTH1R and the G α s protein and the tail phenyl that inserts into the detergent micelle. **g**, Signalling profiles of PTH1R mutants of key residues on PCO371-induced cAMP accumulation. ΔpEC_{50} represents the difference between the negative logarithm of the half-maximum effective

concentration (pEC_{50}) values of the WT and the mutated PTH1Rs. Data from three independent experiments, each of which was carried out in triplicate, are presented as mean \pm s.e.m. Statistical differences were determined by two-sided one-way analysis with Fisher's least significant difference multiple-comparisons test compared with WT ($P < 0.0001$, $P = 0.0002$, $P < 0.0001$, NA , $P = 0.0127$, $P = 0.0005$, $P = 0.0307$, $P = 0.0013$, $P = 0.3160$ and $P = 0.8881$ from R219A to E465A). * $P < 0.05$, ** $P < 0.01$, *** $P < 0.001$ and **** $P < 0.0001$ versus WT receptor; NA, not active; NS, no significant difference.

2.4 Å inward shift at the cytoplasmic end of TM6 as measured by the C α of R400^{6,32b} (in which the superscript annotation refers to the Wootten numbering system for class B GPCRs) and a 2.7 Å outward shift at the cytoplasmic end of TM7 as measured by the C α of Y459^{7,57b} (Extended Data Fig. 5d). Compared to the inactive PTH1R, conformational change triggers a rotation of the TMD helices, resulting in an outward movement at the cytoplasmic end of TM6 (Extended Data Fig. 5e–h). These structural elements are known to be key for G-protein and arrestin binding, and we speculate that they may account for the differential preference for binding of the G protein and arrestin between PTH- and PCO371-bound PTH1R complexes. Together, these observations suggest that PCO371 induced a very distinct PTH1R conformation, unseen for structures of all other class B GPCRs, to couple preferentially with the G protein.

An unusual PCO371-binding site

Within the structure, PCO371 adopted a horizontal U-shape pose that wraps around the bottom half (intracellular half) of TM6 (Fig. 2a–c). The chemical structure of PCO371 comprises the head imidazolidinone, the middle dimethylphenyl, the sulfonamide linker, the piperidine motif, the middle spiro-imidazolone and the tail trifluoromethoxy phenyl (Fig. 1f and Extended Data Fig. 7a). The head imidazolidinone and the middle phenyl of PCO371 are embedded in the interface between the receptor and the G α_s protein and form interactions with the residues within TM2, TM6, TM7 and H8, as well as with the α_5 helix of G α_s (Fig. 2d,e). The head imidazolidinone of PCO371 also forms a hydrogen bond with R219^{2,46b} and a polar interaction with Y391 from the α_5 helix of G α_s . In addition, the head imidazolidinone and the middle phenyl

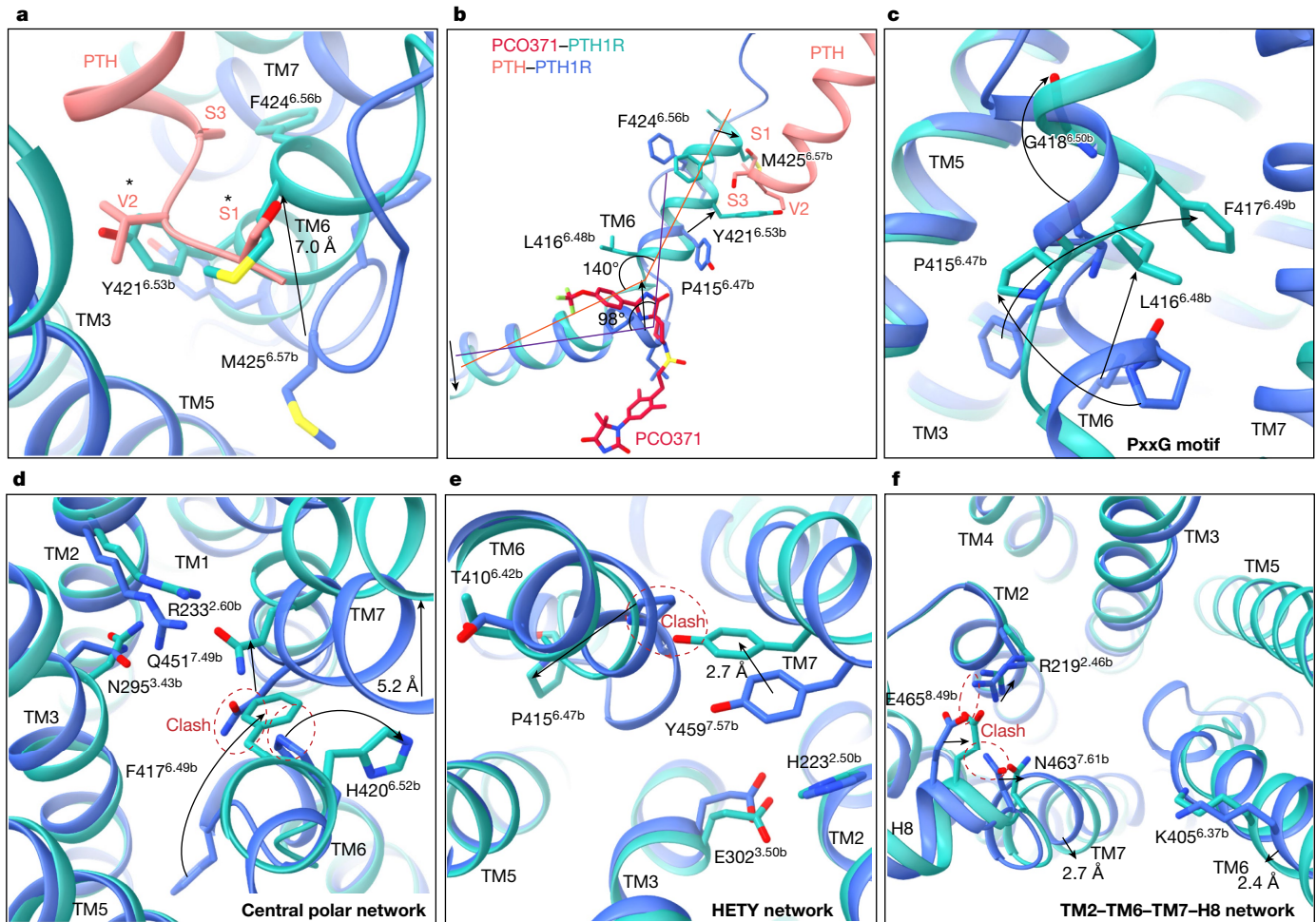


Fig. 3 | Conformational changes of TMD helix bundles during receptor activation between PTH-bound and PCO371-bound PTH1R. **a**, Structural comparison of the TMD bundles of the active PTH1R (light sea green) with PCO371 and PCO371 is omitted for clarity. PTH1R (royal blue) with PTH (light coral) (Protein Data Bank (PDB): 8HAO). G proteins and Nb35 are omitted for clarity. **b**, Comparison of TM6 conformational changes between the

PCO371-bound and PTH-bound PTH1R structures. **c–f**, Different conformations are shown for conserved residues and motifs in the active PTH1R, including the conserved PxxG motif (P415^{6.47b}-L416^{6.48b}-F417^{6.49b}-G418^{6.50b}), the central polar network (R233^{2.60b}-N295^{3.43b}-H420^{6.52b}-Q451^{7.49b}), the HETY network (H223^{2.50b}-E302^{3.50b}-T410^{6.42b}-Y459^{7.57b}) and the TM2-TM6-TM7-H8 network (R219^{2.46b}-K405^{6.37b}-N463^{7.61b}-E465^{8.49b}).

of PCO371 form extensive hydrophobic interactions with the receptor and the α 5 helix of $\text{G}\alpha_s$ (Fig. 2d,e). Specifically, both Y459^{7.57b} and Y391 of $\text{G}\alpha_s$ - α 5 form pi stacking interactions with the middle phenyl of PCO371 (Fig. 2d,e).

In the middle of PCO371, the sulfonamide group forms polar interactions with E302^{3.50b}, and the piperidine group forms hydrophobic contacts with I299^{3.47b} (Fig. 2d,e). The middle spiro-imidazolone group of PCO371 forms hydrogen-bond interactions with the main-chain amine of F417^{6.49b} and the side chain of Y459^{7.57b}. The middle spiro-imidazolone together with the tail phenyl group forms extensive hydrophobic interactions with PTH1R residues from TM3, TM6 and TM7 (Fig. 2d,e). In addition, the tail phenyl inserts into the detergent micelle, and probably interacts with the lipid bilayer in a native system (Fig. 2f). Compared to peptide-bound PTH1R structures, the binding of PCO371 pushes the middle of TM6 outwards by about 5.2 Å as measured by the $\text{C}\alpha$ of P415^{6.47b} to leave space to accommodate PCO371 (arrows in Extended Data Fig. 5b,d).

To investigate the key residues for ligand binding and receptor activation, we assessed PCO371-induced G_s activation by wild-type (WT) and mutant PTH1Rs using cAMP assays. Alanine substitutions in hydrophobic pocket residues (I299^{3.47b}, L413^{6.45b}, P415^{6.47b} and I458^{7.56b}) significantly reduced the potency as measured by pEC_{50} (defined as the negative logarithm of the half-maximum effective concentration) for

PCO371 relative to the WT PTH1R (Fig. 2g, Extended Data Fig. 7b and Extended Data Table 2), indicating that these hydrophobic residues play important roles in transmitting PTH1R G-protein signals. This is in line with the previously reported result that P415^{6.47b} of PTH1R is a key residue for PCO371-mediated PTH1R activation¹⁷. In addition, alanine substitutions of R219^{2.46b} and Y459^{7.57b} showed a great reduction in the potency of PCO371-mediated G_s activation. Alanine substitutions of E302^{3.50b} and H223^{2.50b} also diminished PCO371-induced cAMP production (Fig. 2g, Extended Data Fig. 7b and Extended Data Table 2), which suggests the importance of these residues in PCO371 function. Taken together, the unexpected interface bound by PCO371 between PTH1R and the G protein demonstrates the important roles of individual pocket residues in PCO371 recognition and specificity. Notably, several mutants (V412A, M414A, L416A and F417A) were shown to enhance PCO371 potency (Fig. 2g). Inspecting the structure reveals that the PCO371-binding pocket is relatively narrow and elongated (Fig. 2b,c), and alanine substitutions could leave a larger pocket to reduce the space constraint (or clashes) with PCO371 binding. In addition, most mutations that enhance PCO371 potency are located on TM6, and alanine substitutions (owing to the high helical propensity of alanine³⁶) could stabilize the helical structure, thus stabilizing PCO371 binding. Notably, several alterations, including I299^{3.47b}A, greatly increased basal activation (Extended Data Fig. 7b). The locations of these high

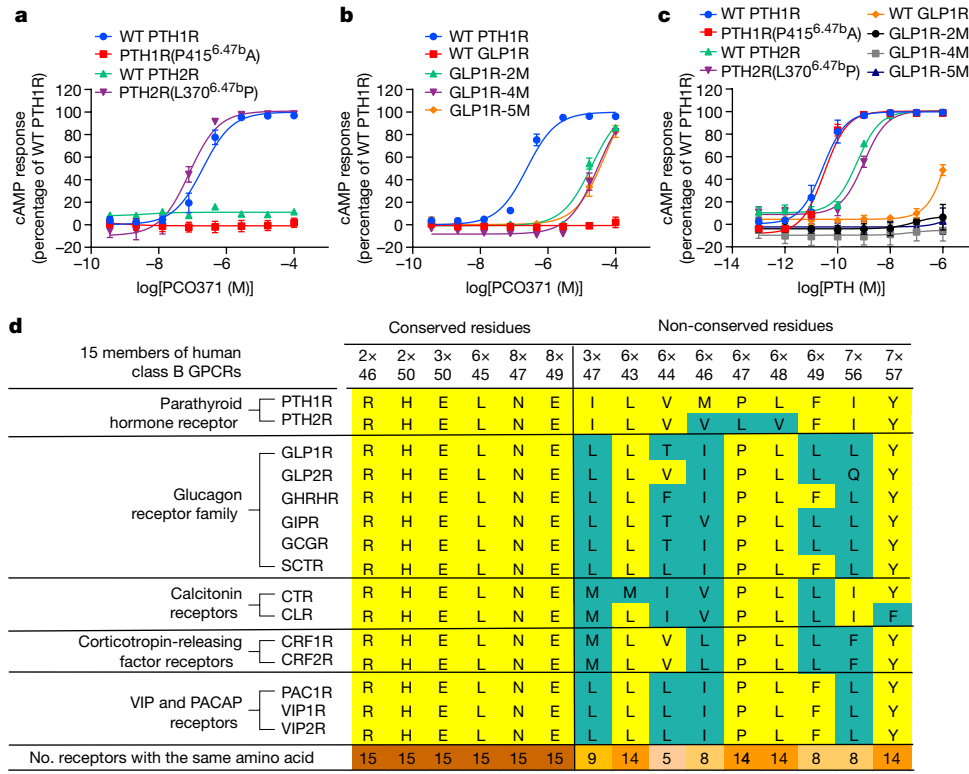


Fig. 4 | Selectivity of PCO371 for PTH1R and the conservation of the PCO371-binding site in class B GPCRs. **a**, Stimulation of cAMP production by PCO371 in the indicated WT and mutant PTH receptors. **b**, Stimulation of cAMP production by PCO371 in the indicated WTs and mutants of GLP1R. Data from three independent experiments ($n=3$), each of which was carried out in triplicate, are presented as mean \pm s.e.m. **c**, Stimulation of cAMP production by PTH in the indicated WT and mutant PTH1R, PTH2R and GLP1R. Data from three

independent experiments ($n=3$) carried out in technical triplicate are presented as mean \pm s.e.m. GLP1R-2M, GLP1R-4M and GLP1R-5M are the combined substitutions of two residues (L244^{3,47b}I and L360^{6,49b}F), four residues (L244^{3,47b}I, T355^{6,44b}V, L360^{6,49b}F and L401^{7,56b}I) and five residues (L244^{3,47b}I, T355^{6,44b}V, L360^{6,49b}F, L401^{7,56b}I and N407^{8,48b}G), respectively. **d**, Sequence alignment of conserved and non-conserved residues forming the PCO371-binding pocket in class B GPCRs.

basal alterations are within the hydrophobic core near the kink of TM6 and these alterations could affect the stability of the inactive state in the same way as the constitutively active alterations in the conserved hydrophilic core³⁷.

PTH1R activation by PCO371

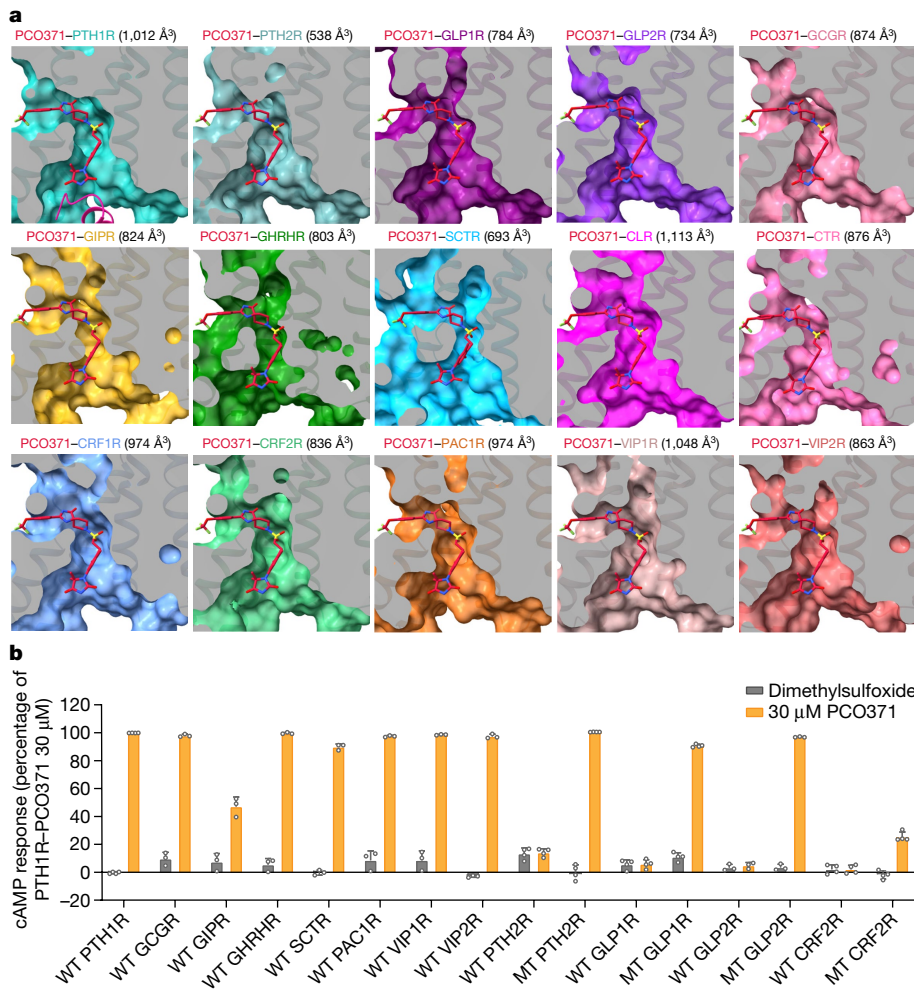
Although all of the active PTH1R structures were solved in the same G-protein-bound state^{23,31,34}, they exhibit conformational differences at their TMD bundles between the PCO371-bound and the PTH-bound PTH1R structures. The most notable observation is a 7.0 Å inward shift at the extracellular end of TM6 in the PCO371-bound PTH1R structure (as measured by the C α of M425^{6,57b}; Fig. 3a), which causes the extracellular end of TM6 (residues M425^{6,57b}, Y421^{6,53b} and F424^{6,56b}) to collide with the PTH amino-terminal residues (S1, V2 and S3; Fig. 3a). This is consistent with the report that PCO371 can inhibit the binding of peptides to their TMD¹⁷. The conserved PxxG motif (P415^{6,47b}–L416^{6,48b}–F417^{6,49b}–G418^{6,50b}) in the middle of TM6 in the PTH-bound PTH1R structure also collides with PCO371 (Fig. 3b); therefore, the PxxG motif in the PCO371–PTH1R–G_s complex structure is shifted outwards to create the binding pocket of PCO371 (Fig. 3b,c). Corresponding to the outward movement of P415^{6,47b} in the PCO371–PTH1R–G_s complex structure, the kink of TM6 at P415^{6,47b} is less pronounced than the TM6 kink in the PTH-bound structure (Fig. 3b), leading to less pronounced outward movement (about 2.4 Å) of TM6 in the cytoplasmic side (Extended Data Fig. 5b).

Compared with the PTH–PTH1R–G_s complex structure, the PCO371–PTH1R–G_s complex structure exhibits large differences in the extracellular half of the TMD structures but retains very similar structure in the intracellular half of the TMD structures (Extended Data Fig. 5b).

Specifically, a large inward movement at the extracellular end of TM6 results in large outward movements at the extracellular ends of TM7 and TM1 (Extended Data Fig. 5c). The rearrangement of these structural elements at the extracellular side results in changes of three conserved polar interaction networks in class B GPCR activation as shown in Fig. 3d–f. The conformational changes of H420^{6,52b} and Q451^{7,49b} in the central polar network of the PCO371-bound PTH1R structure resolve the steric clash with F417^{6,49b}, which is flipped upwards in the PCO371-bound structure from the PTH-bound structure (Fig. 3d). Y459^{7,57b} from the HETY network is shifted upwards and outwards to bind with PCO371. The outward shift of P415^{6,48b} resolves the steric clash with conformational changes of Y459^{7,57b} (Fig. 3e). The outward shift of N463^{7,61b} and E465^{8,49b} from the TM2–TM6–TM7–H8 network also resolves the steric clash with each other, and the clash of E465^{8,49b} with R219^{2,46b} (Fig. 3f). These conformational rearrangements together illustrate the structural changes of PTH1R in response to the change of ligand binding from PTH to PCO371, highlighting the capacity of PTH1R to adopt totally different ligands, which induce very distinct receptor conformations in the peptide-binding pocket. Although the PCO371-bound receptor can coalesce into a very similar intracellular pocket to couple downstream G proteins.

Direct contact of G protein by PCO371

Despite the different binding patterns of the peptide agonists and the small-molecule agonist, PCO371, they both activate PTH1R by inducing a consensus kink in the middle of TM6 and a subsequent outward shift of the cytoplasmic end of TM6 to form a binding cavity for G-protein coupling (Extended Data Fig. 8a,b). Different from the binding modes

**Fig. 5 | A mostly conserved PCO371-like-binding pocket in class B GPCRs.**

a, Structural modelling shows that the PCO371-like-binding pockets are mostly conserved in other members of the class B GPCRs. The volume calculation shows that these pockets are similar in all class B GPCRs. Peptides, G proteins and Nb35 are omitted for clarity. From top left to bottom right, these PDB codes are 8JR9, PTH1R; 7F16, PTH2R; 6X1A, GLP1R; 7D68, GLP2R; 6WPW, GCGR; 7DTY,

GIPR; 7CZ5, GHRHR; 6WZG, SCTR; 6E3Y, CLR; 6NYI, CTR; 6PBO, CRF1R; 6PB1, CRF2R; 6P9Y, PAC1R; 6VN7, VIP1R; 7VQX, VIP2R. **b**, PCO371 has pan-agonist activity in WT and mutant (MT) class B GPCRs. The mutated receptors have two alterations corresponding to the residues in GLP1R that regain response to PCO371. Data are shown as the mean \pm s.e.m. Data are from at least three independent experiments ($n = 3–4$).

of all reported peptides and small-molecule agonists, PCO371 is at the interface between the receptor and the C terminus of $\text{G}\alpha_s$ - $\alpha 5$ in the PCO371-bound PTH1R structure (Extended Data Fig. 8c–e). The C-terminal $\alpha 5$ helix of $\text{G}\alpha_s$ interacts with TM2, TM3, TM5, TM6 and H8 in both the PCO371- and PTH-bound PTH1R structures (Extended Data Fig. 8d–f). In addition, Y391 of $\text{G}\alpha_s$ - $\alpha 5$ forms a π - π interaction with PCO371. E392 and Y391 of $\text{G}\alpha_s$ - $\alpha 5$ also form polar interactions with PCO371 (Extended Data Fig. 8e). These additional interactions are supported by well-resolved density in the cryo-EM map (Extended Data Fig. 8c). The direct contact of PCO371 with both PTH1R and the G protein is consistent with previously reported data¹⁷, which showed that the duration of cAMP response induced by PCO371 is much shorter than that by PTH because PCO371 binds weakly to PTH1R in the absence of a G protein, consistent with the fact that PCO371 acts as a G-protein-biased ligand that lacks arrestin association and subsequent endosomal signalling.

A single residue replacement of L370^{6,47b}P in PTH2R converted it to be activated by PCO371, whereas the P415^{6,47b}A alteration inactivated the response of PTH1R to PCO371 but did not affect its activation by PTH (Fig. 4a,c). It is worth noting that P^{6,47b} is a conserved residue in TM6 of class B GPCRs except for L370^{6,47b} in PTH2R (Fig. 4d), and our data suggest that P^{6,47b} in PTH receptors is a key residue for the selective activation of PTH receptors by PCO371.

Structure-based sequence alignment of class B GPCRs reveals that the PCO371-binding interface has three non-conserved residues between PTH1R and PTH2R and five non-conserved residues between PTH1R and GLP1R (Fig. 4d and Extended Data Fig. 9a–e). In contrast to the single alteration in PTH2R that converts it to respond to PCO371, all single alterations that change the GLP1R residue to the PTH1R residue at the five non-conserved PCO371 pocket residues did not convert GLP1R to respond to PCO371 although the activation of the mutated receptors by the GLP1 peptide was unaffected (Extended Data Fig. 9f–g). Combined pocket alterations of two residues, four residues or five residues can convert the mutated GLP1R to be activated by PCO371 but not by PTH (Fig. 4b,c). The degree of activation of the two-residue-mutated GLP1R by PCO371 is the same as (if not better than) that of the four- or five-residue-mutated GLP1R, suggesting that these two residues are key for PCO371 selectivity.

Selectivity of PCO371 for PTH1R

To investigate the mechanisms underlying the selectivity of PCO371 for PTH1R over other class B GPCRs, we carried out cAMP production assays using transfected WT receptors of PTH1R, PTH2R and GLP1R in AD293 cells. PCO371 did not activate WT PTH2R and GLP1R (Fig. 4a,b).

A conserved PCO371-binding site in class B GPCRs

The ability to enable PCO371 activation through a single residue alteration in PTH2R or a two-residue alteration in GLP1R suggests the possibility of a similar PCO371-binding pocket conserved in other members of the class B GPCRs. To validate this hypothesis, we carried out sequence alignment and homology modelling based on the PCO371-bound PTH1R structure (Figs. 4d and 5a). Sequence alignment reveals that most residues of the 15 PTH1R residues that comprise the PCO371 pocket are conserved across class B GPCRs (Fig. 4d). Structural modelling of all other members of the class B GPCRs suggests the existence of a similar PCO371-binding pocket in these receptors, in which PCO371 could adopt a similar binding mode to that in the PCO371–PTH1R structure (Fig. 5a). To corroborate the sequence and structure analyses, we tested the ability of PCO371 to activate other members of the class B GPCRs (Fig. 5b). In addition to PTH1R, seven WT class B GPCRs (GCGR, GIPR, PAC1R, GHRHR, SCTR, VIP1R and VIP2R) can be activated by PCO371 (Fig. 5b). The WT receptors of GLP1R, GLP2R, PTH2R and CRF2R cannot be activated by PCO371, but one or two substitutions in the pocket residues can convert them to respond to PCO371. On the basis of these results, we conclude that a PCO371-like-binding pocket is mostly conserved in class B GPCRs.

In summary, the structure of the PCO371-bound PTH1R–G_s complex provides a structural basis for small-molecule agonist binding and activation of PTH1R. With reference to PTH, PCO371 is a G-protein-biased ligand that is incapable of arrestin recruitment. The structure reveals that PCO371 binds to an unanticipated agonist-binding site, which induces a conformation that is distinct from that of the PTH-bound PTH1R. The PCO371-binding site is within the TMD at the interface with the G protein, which is far from the receptor ECD; thus, small-molecule agonists at this site do not have to mimic the interactions of peptides with the ECD to promote the binding affinity.

Class B GPCRs have higher sequence homology in their TMDs than in their ECDs, and the PCO371-bound PTH1R structure could serve as a template for small-molecule drug development of class B GPCRs. The findings of our modelling and receptor activation studies suggest that a PCO371-like pocket is probably conserved in most members of the class B GPCRs, thus providing a general direction for structure-based design of small-molecule drugs targeting this new binding site at class B GPCRs.

Online content

Any methods, additional references, Nature Portfolio reporting summaries, source data, extended data, supplementary information, acknowledgements, peer review information; details of author contributions and competing interests; and statements of data and code availability are available at <https://doi.org/10.1038/s41586-023-06467-w>.

- Pal, K., Melcher, K. & Xu, H. E. Structure and mechanism for recognition of peptide hormones by class B G-protein-coupled receptors. *Acta Pharmacol. Sin.* **33**, 300–311 (2012).
- Cong, Z. et al. Structural perspective of class B1 GPCR signaling. *Trends Pharmacol. Sci.* **43**, 321–334 (2022).
- Hollenstein, K. et al. Insights into the structure of class B GPCRs. *Trends Pharmacol. Sci.* **35**, 12–22 (2014).
- de Graaf, C. et al. Extending the structural view of class B GPCRs. *Trends Biochem. Sci.* **42**, 946–960 (2017).
- Grigoriadis, D. E., Hoare, S. R., Lechner, S. M., Slee, D. H. & Williams, J. A. Drugability of extracellular targets: discovery of small molecule drugs targeting allosteric, functional, and subunit-selective sites on GPCRs and ion channels. *Neuropsychopharmacology* **34**, 106–125 (2009).
- Hoare, S. R. Allosteric modulators of class B G-protein-coupled receptors. *Curr. Neuropharmacol.* **5**, 168–179 (2007).
- Koole, C. et al. Recent advances in understanding GLP-1R (glucagon-like peptide-1 receptor) function. *Biochem. Soc. Trans.* **41**, 172–179 (2013).

- Gardella, T. J. & Vilardaga, J. P. International Union of Basic and Clinical Pharmacology. XCI. The parathyroid hormone receptors—family B G protein-coupled receptors. *Pharmacol. Rev.* **67**, 310–337 (2015).
- Cong, Z. et al. Structural basis of peptidomimetic agonism revealed by small-molecule GLP-1R agonists Boc5 and WB4-24. *Proc. Natl Acad. Sci. USA* **119**, e220155119 (2022).
- Griffith, D. A. et al. A small-molecule oral agonist of the human glucagon-like peptide-1 receptor. *J. Med. Chem.* **65**, 8208–8226 (2022).
- Kawai, T. et al. Structural basis for GLP-1 receptor activation by LY3502970, an orally active nonpeptide agonist. *Proc. Natl Acad. Sci. USA* **117**, 29959–29967 (2020).
- Saxena, A. R. et al. Danuglipron (PF-06882961) in type 2 diabetes: a randomized, placebo-controlled, multiple ascending-dose phase 1 trial. *Nat. Med.* **27**, 1079–1087 (2021).
- Ma, H. et al. Structural insights into the activation of GLP-1R by a small molecule agonist. *Cell Res.* **30**, 1140–1142 (2020).
- Thompson, A., Stephens, J. W., Bain, S. C. & Kanamarlapudi, V. Molecular characterisation of small molecule agonists effect on the human glucagon like peptide-1 receptor internalisation. *PLoS ONE* **11**, e0154229 (2016).
- Girdhar, K. et al. Novel insights into the dynamics behavior of glucagon-like peptide-1 receptor with its small molecule agonists. *J. Biomol. Struct. Dyn.* **37**, 3976–3986 (2019).
- Redij, T., Chaudhari, R., Li, Z. Y., Hua, X. X. & Li, Z. J. Structural modeling and in silico screening of potential small-molecule allosteric agonists of a glucagon-like peptide-1 receptor. *ACS Omega* **4**, 961–970 (2019).
- Tamura, T. et al. Identification of an orally active small-molecule PTH1R agonist for the treatment of hypoparathyroidism. *Nat. Commun.* **7**, 13384 (2016).
- Zhao, P. et al. Activation of the GLP-1 receptor by a non-peptidic agonist. *Nature* **577**, 432–436 (2020).
- Zhang, X. et al. Evolving cryo-EM structural approaches for GPCR drug discovery. *Structure* **29**, 963–974 (2021).
- Willard, F. S., Bueno, A. B. & Sloop, K. W. Small molecule drug discovery at the glucagon-like peptide-1 receptor. *Exp. Diabetes Res.* **2012**, 709893 (2012).
- Zhang, X. et al. Differential GLP-1R binding and activation by peptide and non-peptide agonists. *Mol. Cell* **80**, 485–500 (2020).
- Arai, Y. et al. Discovery of novel, potent, and orally bioavailable pyrido[2,3-d][1]benzazepin-6-one antagonists for parathyroid hormone receptor 1. *Bioorg. Med. Chem.* **28**, 115524 (2020).
- Kobayashi, K. et al. Endogenous ligand recognition and structural transition of a human PTH receptor. *Mol. Cell* **82**, 3468–3483 (2022).
- Nishimura, Y. et al. Development of a novel human parathyroid hormone receptor 1 (hPTH1R) agonist (CH5447240), a potent and orally available small molecule for treatment of hypoparathyroidism. *J. Med. Chem.* **61**, 5949–5962 (2018).
- Nishimura, Y. et al. Lead optimization and avoidance of reactive metabolite leading to PCO371, a potent, selective, and orally available human parathyroid hormone receptor 1 (hPTH1R) agonist. *J. Med. Chem.* **63**, 5089–5099 (2020).
- Kolb, P. et al. Community guidelines for GPCR ligand bias: IUPHAR review 32. *Br. J. Pharmacol.* **179**, 3651–3674 (2022).
- Dixon, A. S. et al. NanoLuc complementation reporter optimized for accurate measurement of protein interactions in cells. *ACS Chem. Biol.* **11**, 400–408 (2016).
- Kumari, P. et al. Functional competence of a partially engaged GPCR-beta-arrestin complex. *Nat. Commun.* **7**, 13416 (2016).
- Zhao, F. et al. Structural insights into hormone recognition by the human glucose-dependent insulinotropic polypeptide receptor. *eLife* <https://doi.org/10.7554/eLife.68719> (2021).
- Zhao, L. H. et al. Structure insights into selective coupling of G protein subtypes by a class B G protein-coupled receptor. *Nat. Commun.* **13**, 6670 (2022).
- Zhao, L. H. et al. Structure and dynamics of the active human parathyroid hormone receptor-1. *Science* **364**, 148–153 (2019).
- Ehrenmann, J. et al. High-resolution crystal structure of parathyroid hormone 1 receptor in complex with a peptide agonist. *Nat. Struct. Mol. Biol.* **25**, 1086–1092 (2018).
- Zhao, L. H. et al. Molecular recognition of two endogenous hormones by the human parathyroid hormone receptor-1. *Acta Pharmacol. Sin.* <https://doi.org/10.1038/s41401-022-01032-z> (2022).
- Zhai, X. et al. Molecular insights into the distinct signaling duration for the peptide-induced PTH1R activation. *Nat. Commun.* **13**, 6276 (2022).
- Cary, B. P. et al. Molecular insights into peptide agonist engagement with the PTH receptor. *Structure* <https://doi.org/10.1016/j.str.2023.04.002> (2023).
- Pace, C. N. & Scholtz, J. M. A helix propensity scale based on experimental studies of peptides and proteins. *Biophys. J.* **75**, 422–427 (1998).
- Yin, Y. et al. Rearrangement of a polar core provides a conserved mechanism for constitutive activation of class B G protein-coupled receptors. *J. Biol. Chem.* **292**, 9865–9881 (2017).

Publisher's note Springer Nature remains neutral with regard to jurisdictional claims in published maps and institutional affiliations.

Springer Nature or its licensor (e.g. a society or other partner) holds exclusive rights to this article under a publishing agreement with the author(s) or other rightsholder(s); author self-archiving of the accepted manuscript version of this article is solely governed by the terms of such publishing agreement and applicable law.

© The Author(s), under exclusive licence to Springer Nature Limited 2023

Methods

Constructs of PTH1R and heterotrimeric G proteins

Human PTH1R (residues 27–502) with G188A and K484R substitutions was cloned into the pFastBac vector (Invitrogen) with the haemagglutinin signal peptide (HA), followed by a TEV protease cleavage site and a double MBP (2MBP) and His tag to facilitate expression and purification³¹. To facilitate a stable complex, the LgBiT subunit (Promega) was added to the above PTH1R construct at the C terminus of PTH1R with a 17-amino-acid linker. Based on the published dominant-negative bovine $\text{G}\alpha_s$ (DNG α_s)³¹, a modified bovine $\text{G}\alpha_s$ (mDNG α_s), its N terminus (M1–K25) and α -helical domain (AHD F68–L203) of $\text{G}\alpha_s$ were replaced with the N terminus (M1–M18) and AHD (Y61–K180) of the human $\text{G}\alpha_i$, which can bind scFv16 and Fab_G50 (ref. 38) and the residues N254–T263 of $\text{G}\alpha_s$ were deleted. In addition, eight substitutions (G49D, E50N, L63Y, A249D, S252D, L272D, I372A and V375I) were incorporated to improve the stability of the G-protein subunits³⁹. To facilitate the folding of the G protein, mDNG α_s was coexpressed with GST–RIC8B⁴⁰. Rat $\text{G}\beta_1$ was fused with an SmBiT subunit (peptide 86, Promega)²⁷ after a 15-amino-acid linker at its C terminus. The WT and mutants of PTH1R, PTH2R, GLP1R, GLP2R, GCGR, GIPR, GHRHR, SCTR, PAC1R, VIP1R, VIP2R and CRF2R were cloned into the pcDNA6.0 vector (Promega) for cAMP accumulation. WT PTH1R (27–593), WT β -arrestin 1 (1–393) and WT β -arrestin 2 (1–393) were cloned into the pFB-NanoBiT-G9 expression vector and pcDNA6.0 vector for arrestin recruitment and confocal microscopy. All constructs were cloned using Phanta Max Super-Fidelity DNA Polymerase (Vazyme Biotech).

Expression of PCO371–PTH1R– G_s complex

To facilitate stable complex assembly and purification, PTH1R and G proteins were coexpressed in *Sf9* insect cells (Invitrogen). The *Sf9* cells were grown to a density of 3.5×10^6 cells per millilitre in ESF 921 cell culture medium (Expression Systems) for expression. We infected the cells with five separate virus preparations at a ratio of 1:2:2:2:2, including PTH1R(27–502)–17AA–LgBiT–2MBP, mDNG α_s , $\text{G}\beta_1$ –peptide 86, $\text{G}\gamma_2$ and GST–RIC8B. The infected cells were cultured at 27 °C for 48 h, collected by centrifugation and washed once with PBS. The cell pellets were frozen at –80 °C until further use.

Expression and purification of Nb35

Nanobody-35 (Nb35) was expressed in *Escherichia coli* BL21 cells, and the cultured cells were grown in 2TB medium with 100 µg ml^{–1} ampicillin, 2 mM MgCl₂, 0.1% glucose at 37 °C for 2.5 h until an optical density of 0.7–1.2 at 600 nm was reached. Then the culture was induced with 1 mM IPTG at 37 °C for 4–5 h, and the cells were collected and frozen at –80 °C for further purification. Nb35 was purified by nickel affinity chromatography, followed by size-exclusion chromatography using a HiLoad 16/600 Superdex 75 column or followed by overnight dialysis against 20 mM HEPES, pH 7.4, 100 mM NaCl, 10% glycerol. The Nb35 protein was verified by SDS–polyacrylamide gel electrophoresis and stored at –80 °C.

Purification of PCO371–PTH1R– G_s complex

The complex was purified according to previously described methods^{31,41}. The cell pellets were resuspended in 20 mM HEPES pH 7.4, 100 mM NaCl, 10 mM MgCl₂, 10 mM CaCl₂, 2 mM MnCl₂, 10% glycerol, 0.1 mM TCEP, 15 µg ml^{–1} Nb35, 25 µU ml^{–1} apyrase (Sigma), 200 µM PCO371 (Hefei Fuya Biotechnology), supplemented with protease inhibitor cocktail (TargetMol, 1 ml per 100 ml suspension). The lysate was incubated for 1 h at room temperature and then solubilized in 0.5% (w/v) lauryl maltose neopentylglycol (LMNG, Anatrace) supplemented with 0.1% (w/v) cholestryl hemisuccinate TRIS salt (CHS, Anatrace) for 2 h at 4 °C. The supernatant of the solubilized membranes was collected by centrifugation at 65,000g for 40 min, and then incubated with Dextrin beads 6FF (Smart-lifesciences) for 2 h at 4 °C. The resin was loaded onto

a gravity flow column and washed with 20 column volumes of 20 mM HEPES, pH 7.4, 100 mM NaCl, 10% glycerol, 5 mM CaCl₂, 5 mM MgCl₂, 1 mM MnCl₂, 0.01% (w/v) LMNG, 0.01% glyco-diosgenin (Anatrace) and 0.004% (w/v) CHS, 100 µM PCO371 and 25 µM TCEP. After washing, the protein was cut with TEV protease on a column overnight at 4 °C. The next day, the flowthrough was collected and concentrated, and then the PCO371–PTH1R– G_s flowthrough was loaded onto a Superdex200 10/300 GL column (GE Healthcare), with the buffer consisting of 20 mM HEPES, pH 7.4, 100 mM NaCl, 2 mM MgCl₂, 0.00075% (w/v) LMNG, 0.00025% glyco-diosgenin, 0.0005% (w/v) digitonin (Biosynth), 0.0002% (w/v) CHS, 50 µM PCO371 and 100 µM TCEP. The complex fractions were collected and concentrated for electron microscopy experiments.

Cryo-EM grid preparation and data acquisition

For cryo-EM grid preparation of the PCO371–PTH1R– G_s complex, 3.0 µl purified protein at a concentration of about 4.95 mg ml^{–1} was used for the glow-discharged holey carbon grids (Quantifoil, R1.2/1.3, Au, 300 mesh). The grids were blotted for 2 s at 4 °C, in 100% humidity using a Vitrobot Mark IV (Thermo Fisher Scientific) and then plunge-frozen in liquid ethane. The frozen grid of the PCO371–PTH1R– G_s complex was transferred to a Titan Krios G4 equipped with a Gatan K3 direct electron detector and cryo-EM videos were collected through automatic data collection with super-resolution mode at a pixel size of 0.412 Å using EPU(2.13) at the Advanced Center for Electron Microscopy at Shanghai Institute of Materia Medica, Chinese Academy of Sciences. A total of 8,002 videos were recorded with a pixel size of 0.824 Å at a dose of 50 electrons per Å² for 36 frames. The defocus range of this dataset was –0.8 µm to –1.8 µm. For the dimer complex, another 5,364 videos were obtained with the same parameters.

Cryo-EM data processing

All dose-fractionated image stacks were subjected to beam-induced motion correction by Relion 4.0 (ref. 42). The defocus parameters were estimated by CTFFIND 4.1 (ref. 43) of cryoSPARC-v3.3.1 (ref. 44). For the PCO371–PTH1R– G_s dataset, template auto-picking yielded 7,124,33 particles, which were processed for two rounds by reference-free two-dimensional classification using cryoSPARC⁴⁴. With the initial model, after two rounds of three-dimensional classification using Relion, local masks were used on the receptor. A total of 1,099,315 particles were used for further refinement and polishing. Particle subtraction was used to subtract the density of the micelle from the signal of the complex and for refinement, yielding reconstructions with a global resolution of 2.57 Å, which were subsequently post-processed by DeepEMhancer⁴⁵.

Model building and refinement

The cryo-EM structure of the long-acting-PTH1R– G_s –Nb35 complex (PDB code 6NBF) was used as the initial model for model building and refinement against the electron microscopy map. The model was docked into the electron microscopy density map using Chimera⁴⁶, followed by iterative manual adjustment and rebuilding in COOT 0.9.6 (ref. 47). Real-space and Rosetta refinements were carried out using Phenix 1.20 (ref. 48). The fit of the refined model to the final map was analysed using model-versus-map FSC. To monitor the potential overfitting in model building, FSC_{work} and FSC_{free} were determined by refining ‘shaken’ models against unfiltered half-map-1 and calculating the FSC of the refined models against unfiltered half-map-1 and half-map-2. The final refinement statistics are provided in Extended Data Table 1. Structural figures were prepared in Chimera 1.14 and Chimera X1.3 and PyMOL 2.5.2 (<https://pymol.org/2/>).

Modelling and volume calculation

The homology modelling of class B GPCRs was based on the PTH1R structure using MODELLER (10.2)⁴⁹. The sequence of PTH1R in our

cryo-EM structure was used as the reference sequence. After alignment from the receptor sequence from other class B GPCR structures, AutoModel of MODELLER was applied for homology modelling. The structure with the lowest discrete optimized protein energy potential was used for the following volume calculation using PyVOL (1.7.8)⁵⁰. In volume calculation, the minimum radius was 1.2, and the maximum radius was 3.4. The pocket was defined as the residues around 5 Å of the ligand, and during calculation, the Gα protein of PTH1R was included.

cAMP accumulation assay

PTH-, PCO371-, TIP39- and GLP1-stimulated cAMP accumulations were measured by a LANCE Ultra cAMP kit (PerkinElmer). After 24-h culture, the transfected AD293 cells (Agilent) were seeded into 384-well microtitre plates at a density of 3,000 cells per well in HBSS supplemented with 5 mM HEPES, 0.1% (w/v) BSA or 0.1% (w/v) casein and 0.5 mM 3-isobutyl-1-methylxanthine. The cells were stimulated with different concentrations of peptide agonists for 30 min at room temperature. Eu-cAMP tracer and ULight-anti-cAMP were then diluted by cAMP detection buffer and added to the plates separately to terminate the reaction. Plates were incubated at room temperature for 15 min and the fluorescence intensity was measured at 620 nm and 665 nm by an EnVision multilabel plate reader (PerkinElmer).

NanoBiT β-arrestin recruitment assay

The recruitment of PTH1R to β-arrestin was detected in HEK293 cells (ATCC) using the NanoLuc Binary System (NanoBiT; Promega). The LgBiT subunit was fused to the C terminus of PTH1R and the SmBiT subunit was fused to the N terminus of WT β-arrestin 1 (1–393) and WT β-arrestin 2 (1–393). The HEK293 cells were collected and plated into 384-well microtitre plates at a density of 3,000 cells per well 24 h after co-transfection of PTH1R-LgBiT and SmBiT-β-arrestin. Coelenterazine was then added to the plates in the dark with the final concentration of 10 μM (5 μl per well). The ligands of different concentrations were finally added to the plates and then the bioluminescence signal was measured using an EnVision plate reader (PerkinElmer).

Confocal microscopy

HEK293 cells were seeded on coverslips in 12-well plates (1×10^5 cells per well) in DMEM medium (supplemented with 10% fetal bovine serum) at 37 °C under 5% CO₂. For protein expression, cells were transfected with the indicated plasmids (500 ng PTH1R and 500 ng β-arrestin) using FuGENE HD transfection reagent (Promega), at a 1:3 ratio of DNA to transfection reagent. After transfection for 24 h, cells were stimulated with 10 μM different ligands or PBS (vehicle) for 5 min, and then fixed with 4% paraformaldehyde and permeabilized with PBS/0.3% Triton X-100 for 20 min. For nuclear staining, all slices were counterstained with 4',6-diamidino-2-phenylindole solution for 15 min and then washed with PBS. Coverslips were mounted onto glass slides before imaging using an LSM 900 confocal microscope, and the data were analysed by Zeiss ZEN 3.0 (blue edition).

Surface expression assay

WT PTH1R and its mutants were cloned into pcDNA6.0 (Invitrogen) with 3× Flag tag at the C terminus and their cell-surface expression was determined by flow cytometry. AD293 cells were collected after 24 h of transient transfection and then blocked with 5% BSA in PBS at room temperature for 15 min followed by incubation with primary mouse anti-Flag antibody (1:100) at room temperature for 1 h. The cells were then washed three times with PBS containing 1% BSA and incubated with anti-mouse Alexa-488-conjugated secondary antibody (1:1,000) at 4 °C in the dark for 1 h. After another three

washes, the cells were resuspended with 500 μl PBS containing 1% BSA for detection in an ACEA NovoCyte 3000 flow cytometer system (Agilent Biosciences) with excitation of 488 nm and emission of 530 nm. The cells were gated with a forward scatter cutoff setting a gain value of 0.18 by using the blank sample as the reference value for the background fluorescence signal. The left region represents the negative cell community (FITC⁻), whereas the right region represents the positive cell community (FITC⁺). For each sample, data for approximately 8,000 cellular events were collected, and these were analysed using NovoExpress software (1.4.0) and normalized to WT PTH1R.

Statistical analysis

All functional data are shown as means ± s.e.m. Statistical analysis was carried out using GraphPad Prism 8.0 (GraphPad Software). Experimental data were evaluated with a three-parameter logistic equation. The significance was determined with either two-tailed Student's *t*-test or one-way analysis of variance. *P*<0.05 was considered statistically significant.

Reporting summary

Further information on research design is available in the Nature Portfolio Reporting Summary linked to this article.

Data availability

A cryo-EM map has been deposited in the Electron Microscopy Data Bank under the accession code EMD-36593 (PCO371-bound PTH1R-G_s complex). The atomic coordinates have been deposited in the PDB under the accession code 8JR9 (PCO371-bound PTH1R-G_s complex).

38. Maeda, S. et al. Development of an antibody fragment that stabilizes GPCR/G-protein complexes. *Nat. Commun.* **9**, 3712 (2018).
39. Nehme, R. et al. Mini-G proteins: novel tools for studying GPCRs in their active conformation. *PLoS ONE* **12**, e0175642 (2017).
40. Chan, P. et al. Purification of heterotrimeric G protein α subunits by GST-Ric-8 association: primary characterization of purified Gα_{olf}. *J. Biol. Chem.* **286**, 2625–2635 (2011).
41. Ma, S. et al. Molecular basis for hormone recognition and activation of corticotropin-releasing factor receptors. *Mol. Cell* **77**, 669–680 (2020).
42. Zivanov, J., Nakane, T. & Scheres, S. H. W. Estimation of high-order aberrations and anisotropic magnification from cryo-EM data sets in RELION-3.1. *IUCrJ* **7**, 253–267 (2020).
43. Rohou, A. & Grigorieff, N. CTFFIND4: fast and accurate defocus estimation from electron micrographs. *J. Struct. Biol.* **192**, 216–221 (2015).
44. Punjani, A., Rubinstein, J. L., Fleet, D. J. & Brubaker, M. A. cryoSPARC: algorithms for rapid unsupervised cryo-EM structure determination. *Nat. Methods* **14**, 290–296 (2017).
45. Sanchez-Garcia, R. et al. DeepEMhancer: a deep learning solution for cryo-EM volume post-processing. *Commun. Biol.* **4**, 874 (2021).
46. Pettersen, E. F. et al. UCSF Chimera—a visualization system for exploratory research and analysis. *J. Comput. Chem.* **25**, 1605–1612 (2004).
47. Emsley, P. & Cowtan, K. Coot: model-building tools for molecular graphics. *Acta Cryst. D* **60**, 2126–2132 (2004).
48. Adams, P. D. et al. PHENIX: a comprehensive Python-based system for macromolecular structure solution. *Acta Cryst. D* **66**, 213–221 (2010).
49. Webb, B. & Sali, A. Comparative protein structure modeling using MODELLER. *Curr. Protoc. Bioinformatics* **54**, 5.6.1–5.6.37 (2016).
50. Smith, R. H. B., Dar, A. C. & Schlessinger, A. PyVOL: a PyMOL plugin for visualization, comparison, and volume calculation of drug-binding sites. Preprint at bioRxiv <https://doi.org/10.1101/816702> (2019).

Acknowledgements The cryo-EM data were collected at the Advanced Center for Electron Microscopy at the Shanghai Institute of Materia Medica, the Chinese Academy of Sciences (CAS). This work was supported by the CAS Strategic Priority Research Program (XDB37030103 to H.E.X.); the Young Innovator Association of the CAS (2018325 and Y2022078 to L.-H.Z. and 2019282 to K.Wang); the National Natural Science Foundation of China (32071203 to L.-H.Z.; 32130022 and 82121005 to H.E.X.); the National Key R&D Program of China (2019YFA0904200) and the SA-SIBS Scholarship Program to L.-H.Z.; the Shanghai Municipal Science and Technology Major Project (2019SHZDXZ02 to H.E.X. and 23ZR1475200 to L.-H.Z.); State Key Laboratory of Drug Research (SKLDR-2023-TT-04).

Author contributions L.-H.Z. designed the expression constructs, purified the complexes, prepared the final samples for collection of cryo-EM data relating to the structure, prepared the cryo-EM grids, participated in model building and function assays, carried out structure

Article

and function data analysis, prepared figures and wrote the manuscript; W.H. and K.Wu collected the cryo-EM data, Q.Y. and J.L. carried out map calculations, Q.Y. and H.S. built and refined the structure models; X.H. carried out structure modelling and volume calculation; L.-H.Z., Q.H., Y.G. and Y.L. constructed functional plasmids, Q.H. carried out signalling experiments under the supervision of L.-H.Z.; K.Wang, and J.S. supplied materials; L.-H.Z. and H.E.X. conceived the project and wrote the manuscript.

Competing interests H.E.X. is a founder of Cascade Pharmaceuticals. All other authors declare no competing interests.

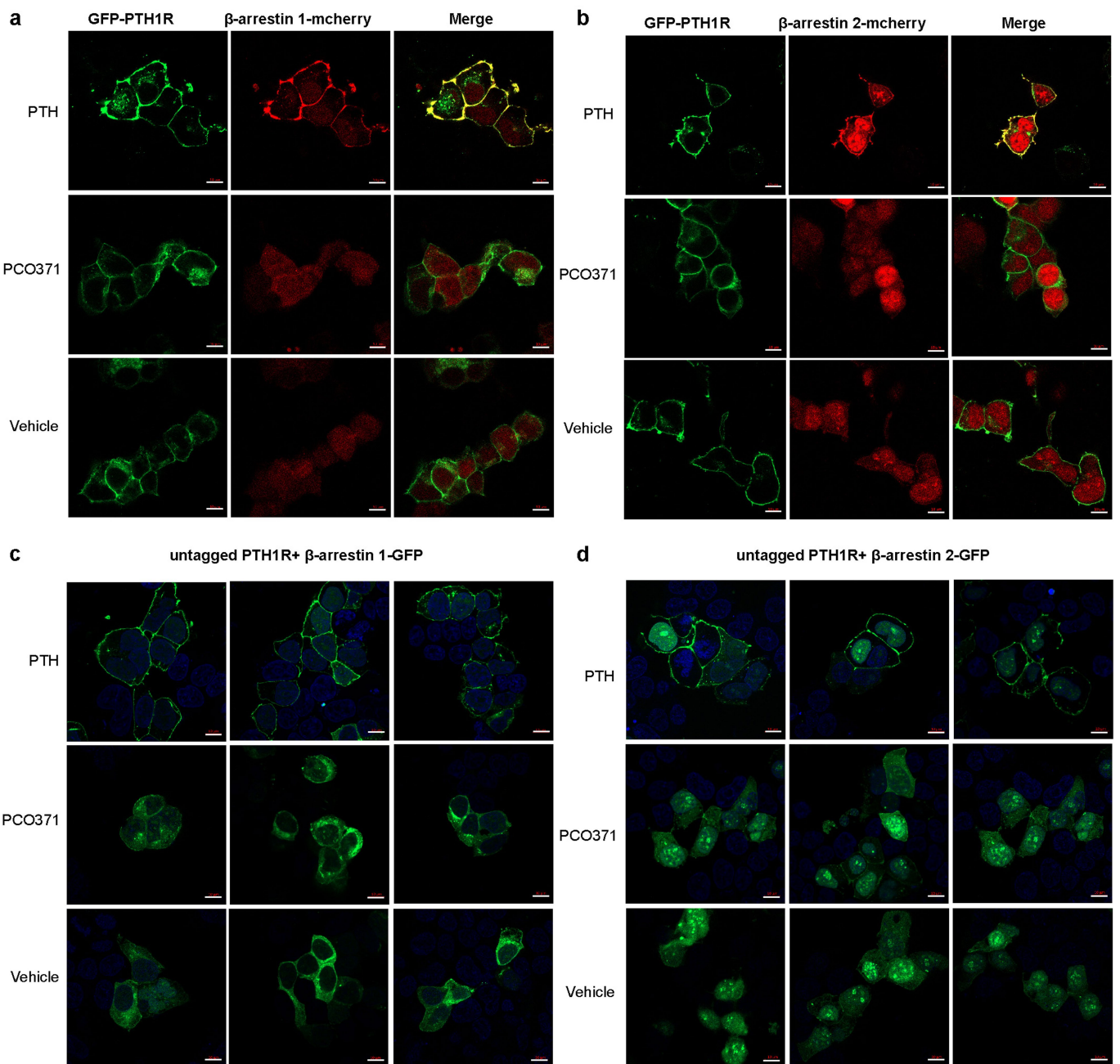
Additional information

Supplementary information The online version contains supplementary material available at <https://doi.org/10.1038/s41586-023-06467-w>.

Correspondence and requests for materials should be addressed to Li-Hua Zhao or H. Eric Xu.

Peer review information *Nature* thanks Sudarshan Rajagopal and the other, anonymous, reviewer(s) for their contribution to the peer review of this work. Peer reviewer reports are available.

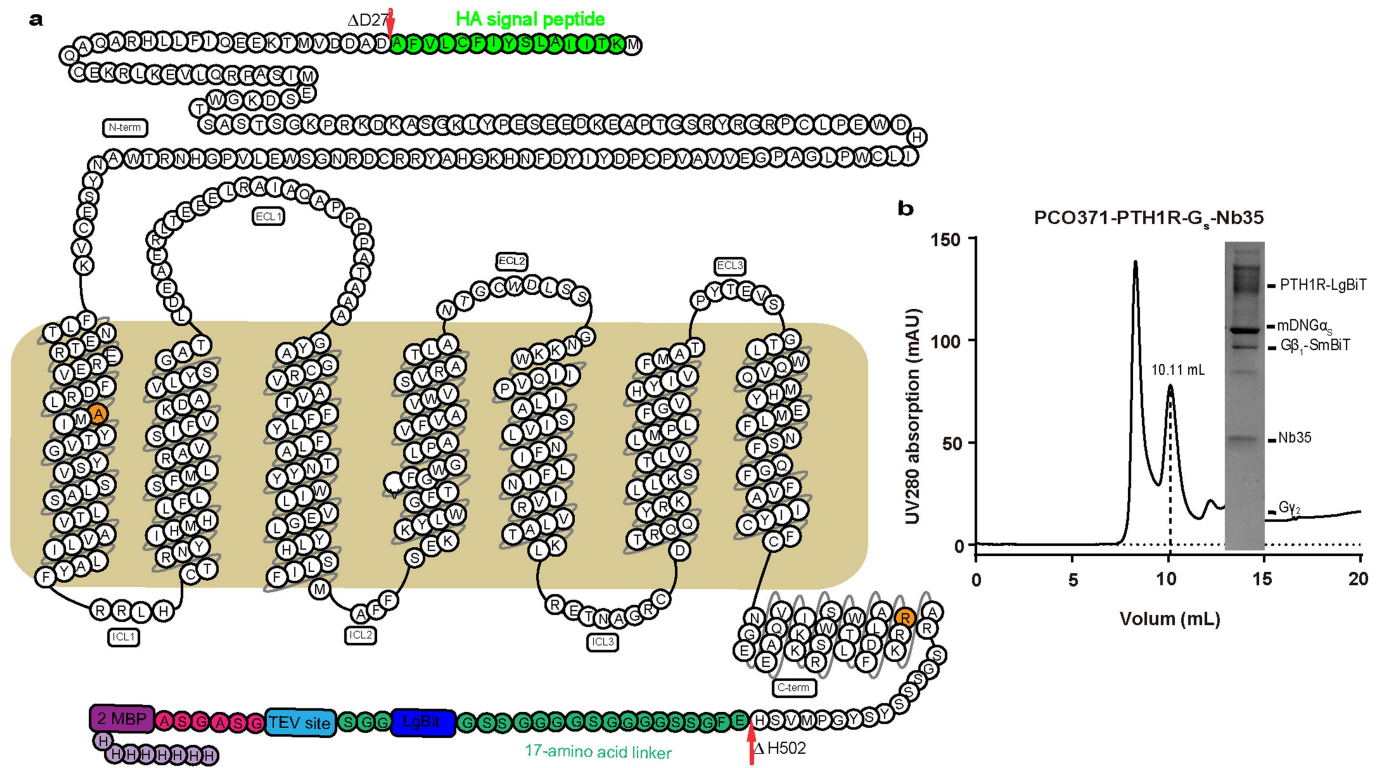
Reprints and permissions information is available at <http://www.nature.com/reprints>.



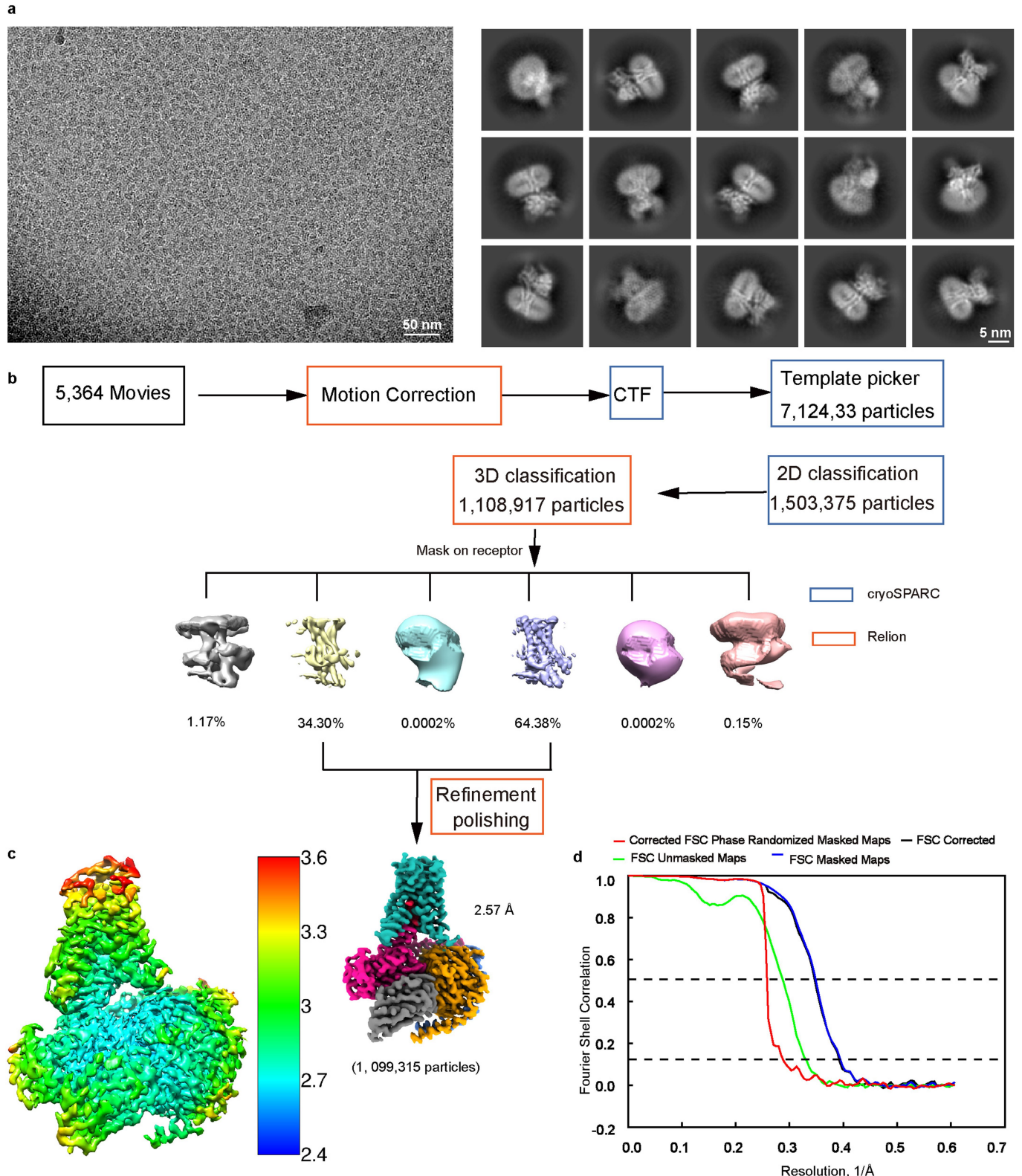
Extended Data Fig. 1 | Confocal microscopy of HEK-293 cells expressing PTH1R with β -arrestin-mcherry. (a–b) The cells expressing GFP-PTH1R (green) with β -arrestin-mcherry (red) and treated with PTH or PCO371 (5 min) were shown with significant recruitment of both β -arrestin 1 and β -arrestin 2 to the cell membranes after PTH stimulation (top row), whereas PCO371 and vehicle control did not stimulate membrane association of both β -arrestin 1 and

β -arrestin 2 (middle and bottom row). (c–d) HEK-293 cells coexpressing untagged PTH1R and β -arrestin-GFP and treated with PTH (5 min) had significant recruitment of both β -arrestin 1 and β -arrestin 2 to cell membranes (top row). While β -arrestin-GFP (green) appeared diffuse in cells treated with PCO371 stimulation and untreated control (vehicle) (middle and bottom row). Data are from three independent experiments ($n = 3$). Scale bar, 10 μ m.

Article

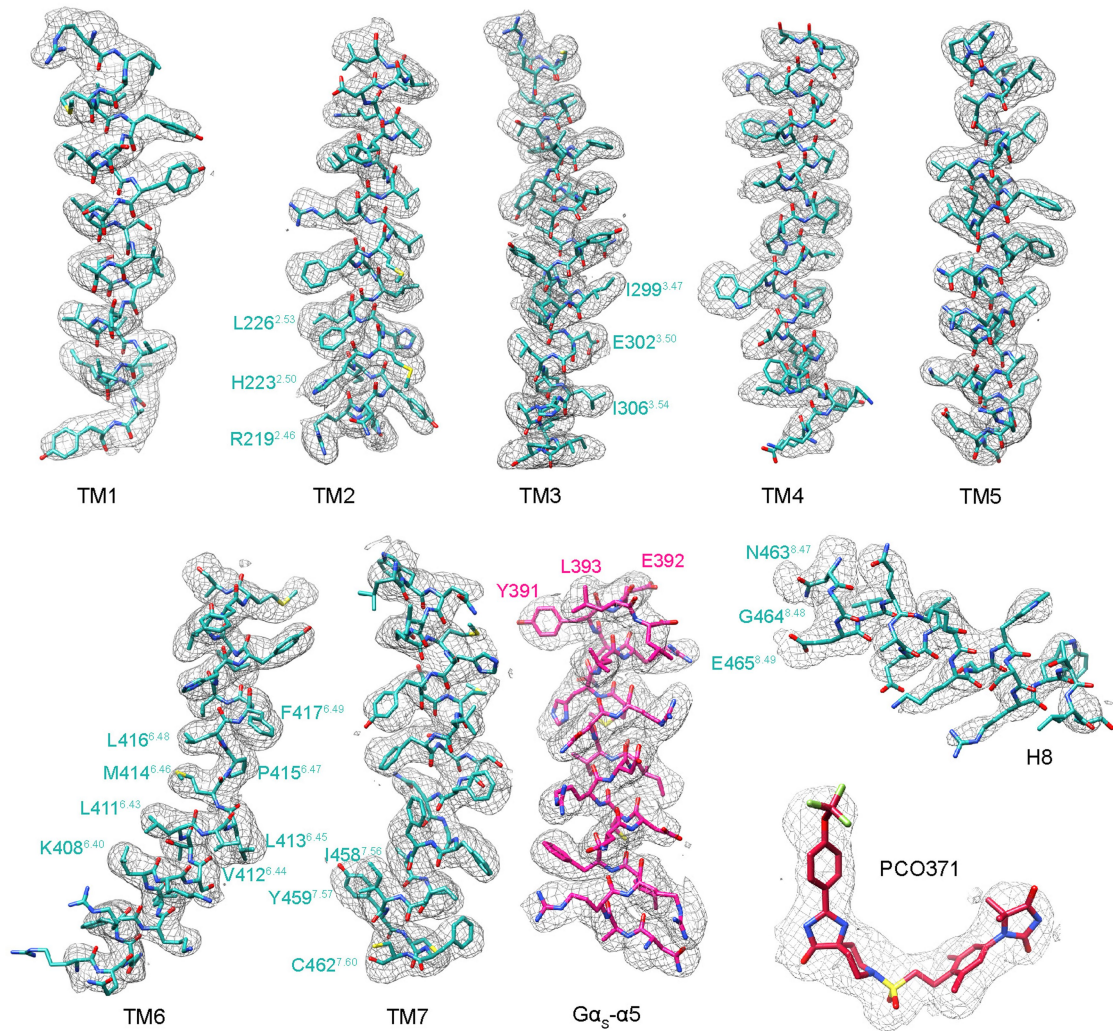


Extended Data Fig. 2 | Construct of receptor and purification of the PCO371-PTH1R-G_s complex. (a) Snake plot diagram of the PTH1R-LgBiT construct. (b) The size-exclusion chromatography elution profile on Superdex200 Increase 10/300GL (left panel) and SDS-PAGE analysis (right panel) of the PCO371-PTH1R-G_s complex.



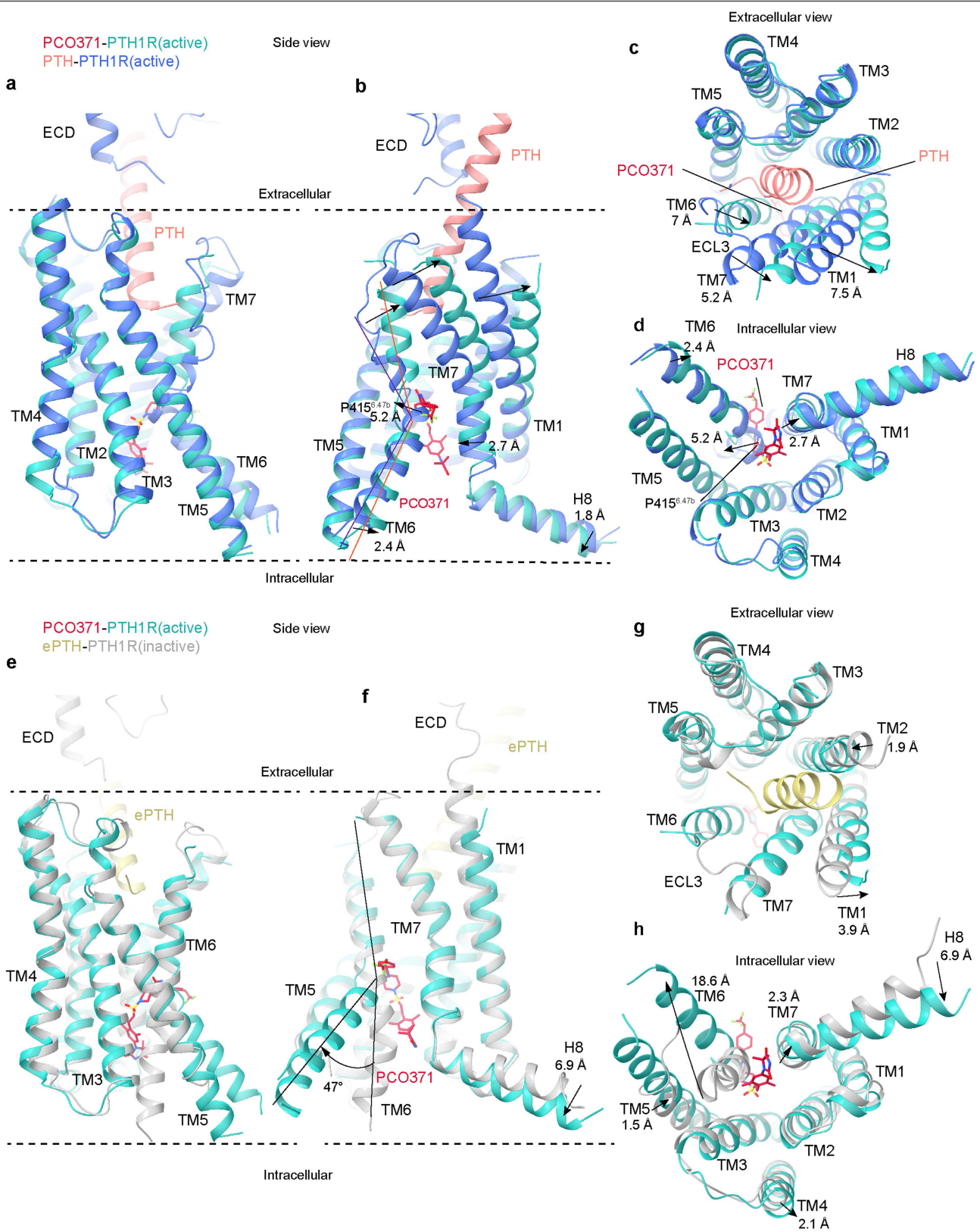
Extended Data Fig. 3 | Single particle cryo-EM data analysis of the PCO371-PTH1R-G_s complex. (a) Representative cryo-EM micrograph from 5364 movies of the PCO371-PTH1R-G_s complex and representative 2D class averages with distinct secondary structure features from different views. (b) Data processing

flowchart of PCO371-PTH1R-G_s complex by CryoSPARC and Relion. (c) Color cryo-EM map of the PCO371-PTH1R-G_s complex, showing local resolution (Å) calculated using Relion. (d) “Gold-standard” FSC curve of the PCO371-PTH1R-G_s complex, with the global resolution defined at the FSC = 0.143 is 2.57 Å.



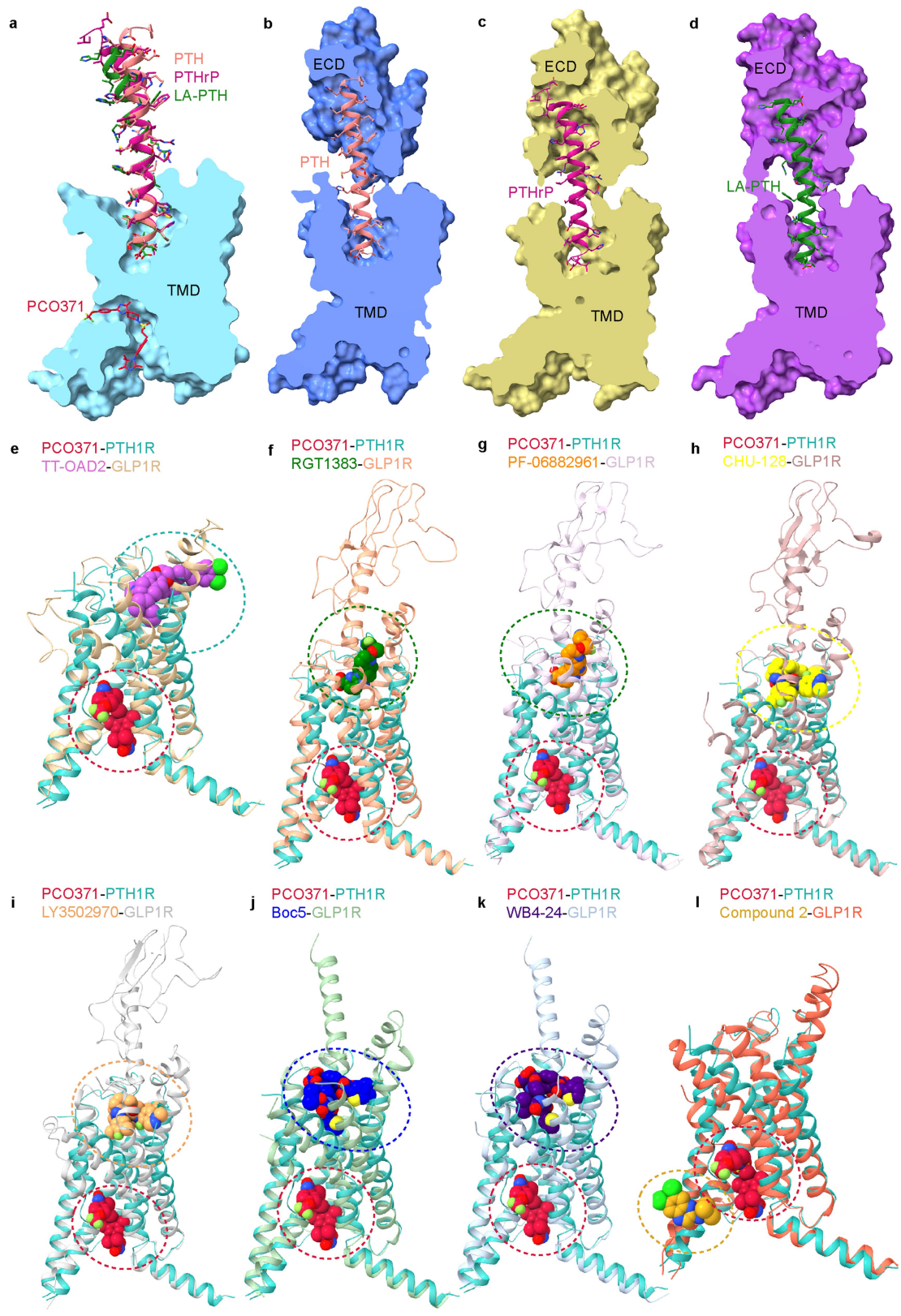
Extended Data Fig. 4 | Cryo-EM density maps of the PCO371-PTH1R-G_s protein structures. Cryo-EM density map and the model of the PCO371-PTH1R-G_s structure are shown for all transmembrane helices and helix 8

of PTH1R, PCO371, and Gα_s-α5 helix. The model is shown in stick representation. All of them display good density.



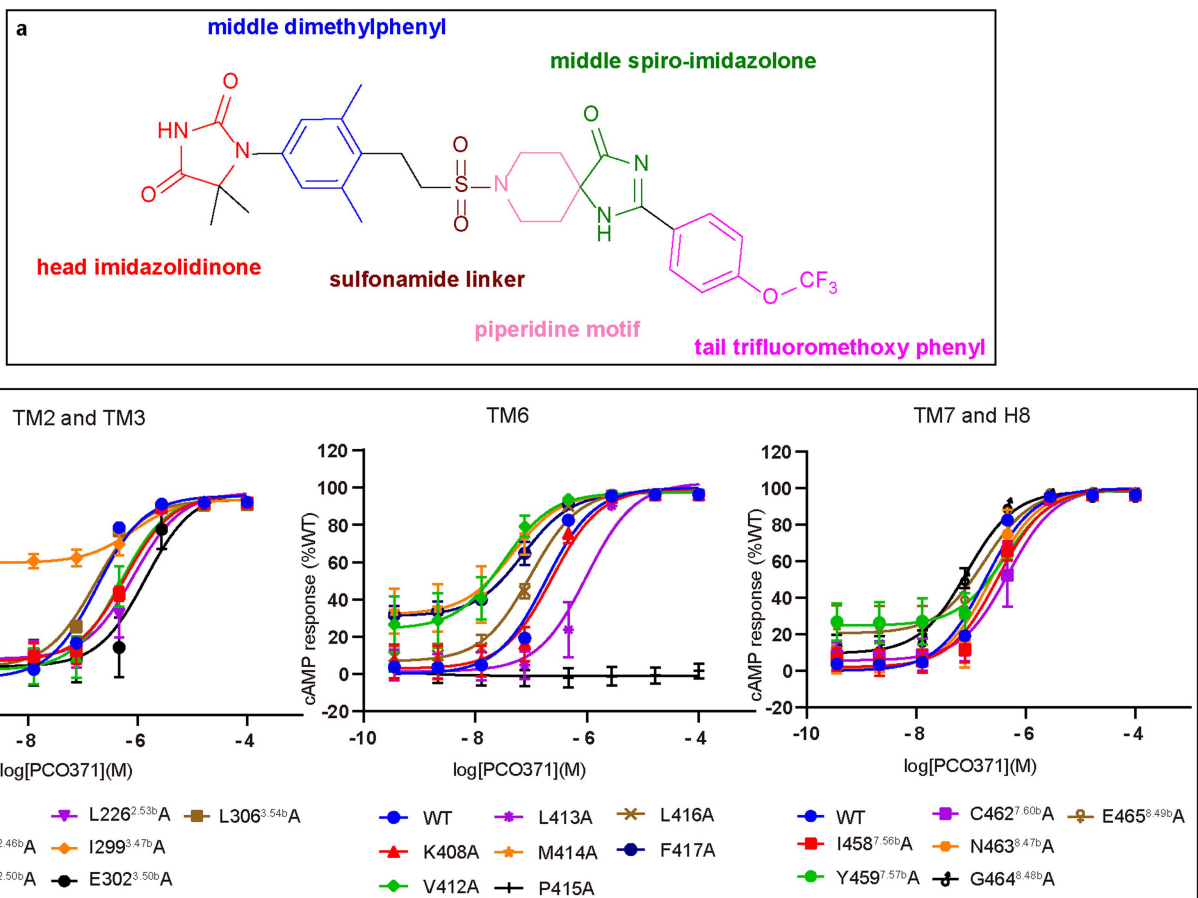
Extended Data Fig. 5 | Structure comparisons of the active state and inactive state of PTH1R induced by different ligands. (a-d) Structure comparisons are between the active state complexes with PTH and with PCO371. Superimposition of PTH1R from PDB: 8HA0 (PTH1R: royal blue, PTH: light coral) and the PCO371-bound PTH1R structure (PTH1R: light sea green, PCO371: crimson) reveals different peptide- and PCO371-binding sites. (a-b) Side view of different binding pockets and conformational changes in receptors; (c) Extracellular view and

(d) intracellular view of PTH1R conformational changes. (e-h) Superimposed structures of PCO371-bound PTH1R in the active state, and ePTH-bound PTH1R in the inactive state from PDB: 6FJ3 (PTH1R: dark gray, ePTH: dark khaki) and the PCO371-bound PTH1R structure (PTH1R: light sea green, PCO371: crimson). (e-f) Side view of different binding pockets and conformational changes in receptors; (g) Extracellular view and (h) intracellular view of PTH1R conformational changes.

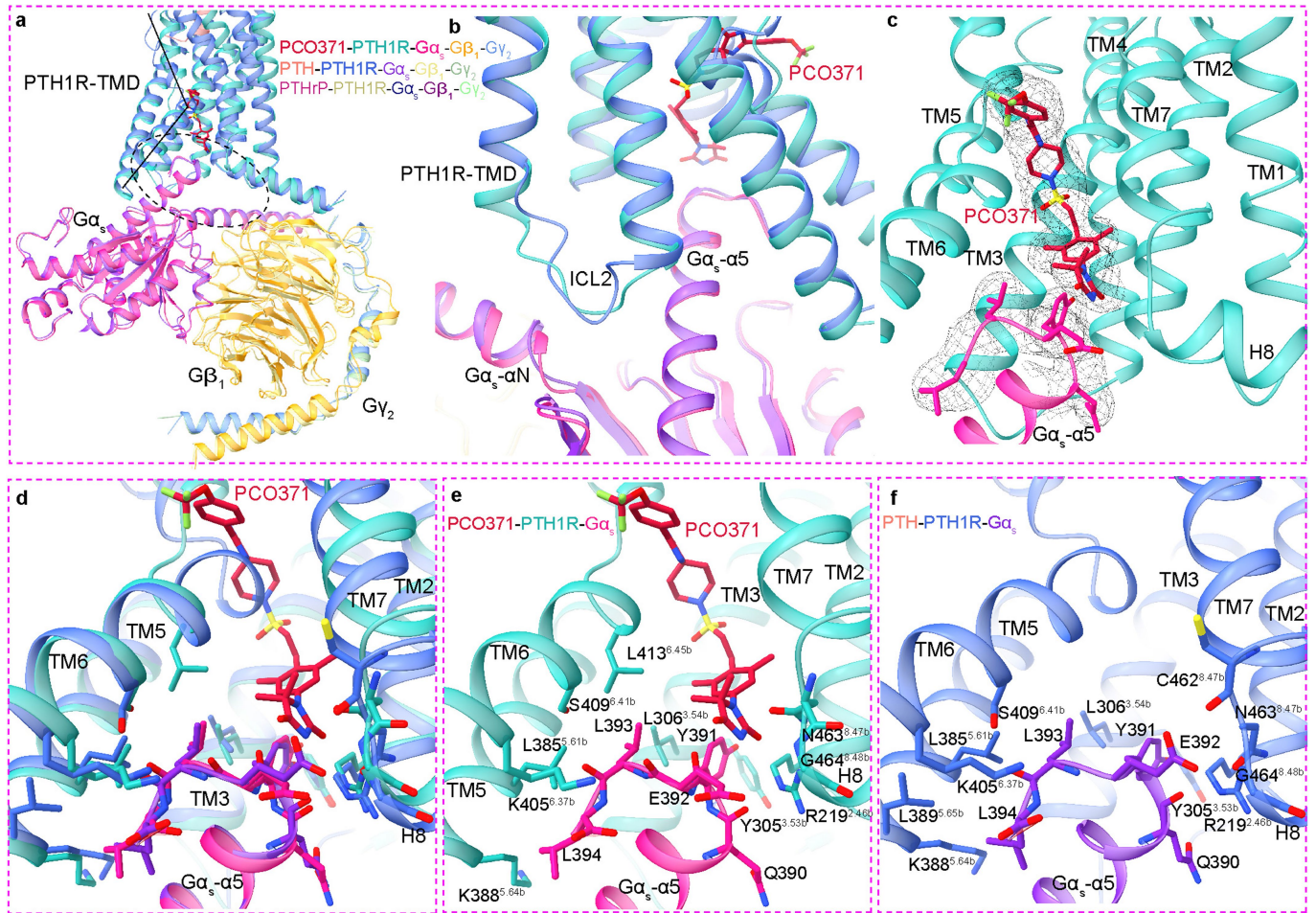
**Extended Data Fig. 6** | See next page for caption.

Extended Data Fig. 6 | Comparisons of peptide hormone binding pockets and small molecule agonist binding sites of class B GPCRs. The PCO371 binding pocket is different from both peptide binding pockets and other small molecule binding pockets of class B GPCRs. **(a–d)** Comparisons the ligand-binding pockets between PCO371 and peptides of PTH1R. The receptor is shown in surface representation and colored in light sea green and PCO371 in crimson is shown as sticks. In three PTH-, PTHrP- and LA-PTH-bound PTH1R-G_s complex structures, the receptors are shown in surface representation and colored in royal blue, dark khaki and dark orchid, respectively. PTH, PTHrP and LA-PTH are colored in light coral, medium violet red and forest green, respectively. They are shown as sticks and ribbon (PDB: 8HA0, 8HAF and 6NBF). G proteins and Nb35 are omitted for clarity. **(e–l)** Comparisons of small

molecule agonist binding sites of class B GPCRs. Superimposition of the PTH1R (light sea green) in complex with G_s bound to PCO371 (crimson) with the GLP1R in complexes with G_s bound to different non-peptidic ligands, including small molecule agonists: TT-OAD2(PDB: 6ORV; TT-OAD2: dark orchid, GLP1R: burly wood); RGT1383 (PDB: 7C2E; RGT1383: green, GLP1R: light salmon); PF-06882961(PDB: 6X1A; PF-06882961: dark orange, GLP1R: thistle); CHU-128 (PDB: 6X19; CHU-128: yellow, GLP1R: rosy brown); LY3502970 (PDB: 6XOX; LY3502970: sandy brown, GLP1R: silver); Boc5 (PDB: 7X8R; Boc5:blue, GLP1R: dark sea green) and WB4-24 (PDB: 7X8S; WB4-24: indigo, GLP1R: light steel blue) and with an allosteric ligand, Compound 2, (PDB: 7EVN; Compound 2: goldenrod, GLP1R: tomato), G proteins and Nb35 are omitted for clarity.



Extended Data Fig. 7 | Chemical structure of PCO371 and PCO371-mediated cAMP production by receptors containing alanine mutants of key residues in PCO371 binding pocket. (a) The chemical structure of PCO371 is comprised of the head imidazolidinone, the middle dimethylphenyl, the sulfonamide linker, the piperidine motif, the middle spiro-imidazolone, and the tail trifluoromethoxy phenyl. (b) PCO371-mediated cAMP production by receptors containing alanine mutants of key residues within TM2, TM3, TM6, TM7 and H8. Data from three independent experiments ($n = 3$) performed in technical triplicate are presented as mean \pm s.e.m.

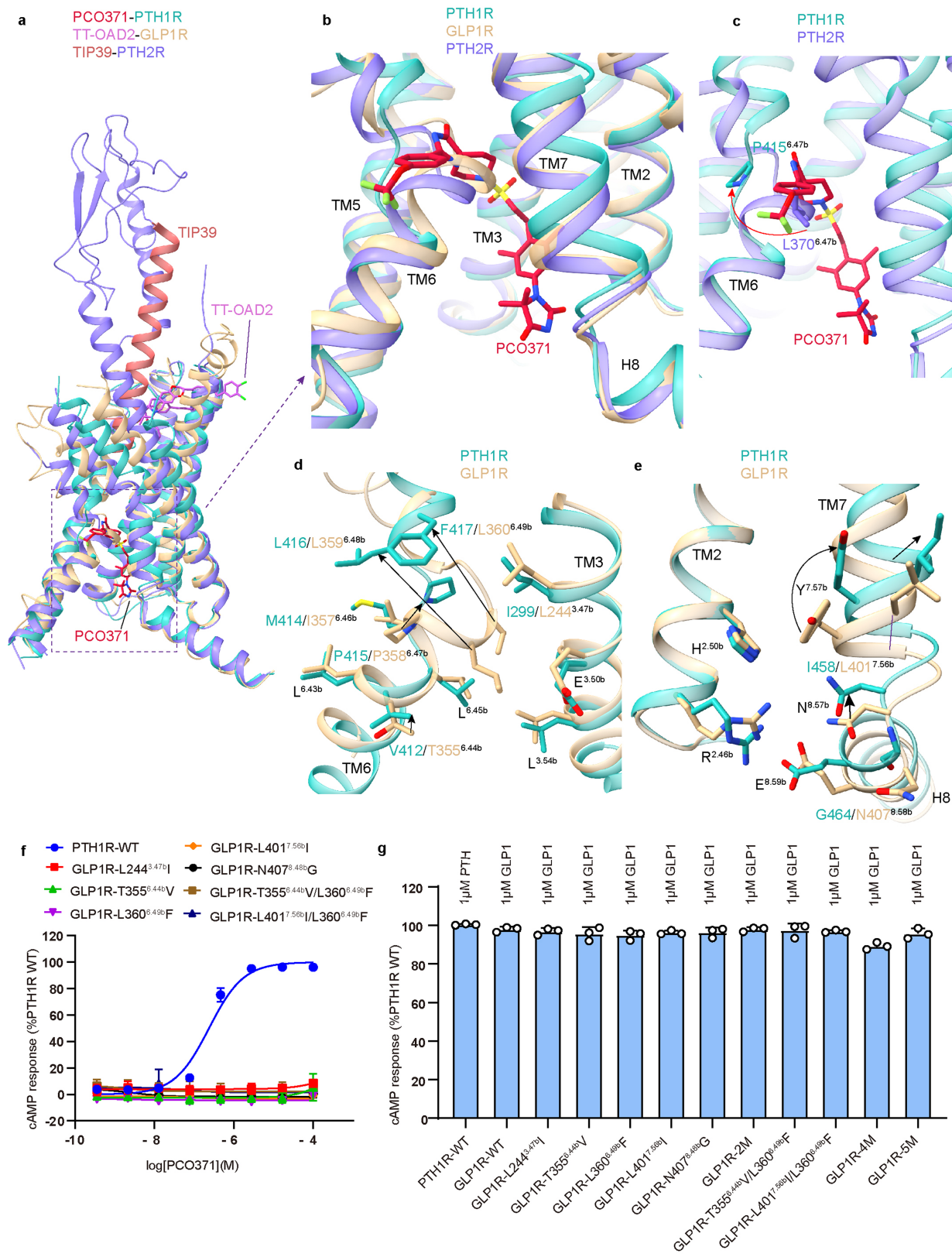


Extended Data Fig. 8 | The similarity and the difference of PTH1R in G protein-coupling by hormone peptide and small molecule agonist.

(a) Structural comparison of G protein in different ligands bound PTH1R-G α_s complex structures. (b) Close up of the α N and G α_s - α 5 helix of G α_s , which form interactions with ICL2 and TMD helix bundles in all G protein bound complex structures, showing similar G protein conformation, but the noteworthy

difference is that the C-terminal of G α_s - α 5 helix makes additional interactions with the small molecule agonist. (c) Good cryo-EM density supports ligand interact with G α_s . (d-f) The similar set of interactions between the C-terminal of G α_s - α 5 helix with the receptor. E392 shifts outward due to steric clash. Y391, E392, and L393 form additional interactions with PCO371.

Article



Extended Data Fig. 9 | Key residues for PCO371 selectivity among class B GPCRs. (a) Structural comparison of receptors and ligands among PCO371-PTH1R-Gs and TT-OAD2-GLP1R-Gs and TIP39-PTH2R-Gs complexes. (a-b) Structural comparison of the cytoplasmic regions of PTH1R, PTH2R and GLP1R during the receptor activation. (c) Structural comparison of P415^{6.47b} and L370^{6.47b} in PTH receptors. (d-e) Different conformations of residues in the active PTH1R, and GLP1R that are involved the interface of PCO371 in receptor

activation. (f) Stimulation of cAMP production by PCO371 in the WT and mutants of GLP1R. Data from three independent experiments ($n = 3$) performed in technical triplicate are presented as mean \pm s.e.m. (g) Stimulation of cAMP production by the cognate ligands of PTH1R, PTH2R and GLP1R in mutants of receptors. Data from three independent experiments ($n = 3$) performed in technical triplicate are presented as mean \pm s.e.m.

Extended Data Table 1 | Cryo-EM data collection, refinement and validation statistics

PCO371-PTH1R-G _s -complex (EMD-36593) (PDB: 8JR9)	
Data collection and processing	
Magnification	105000
Voltage (kV)	300
Electron exposure (e-/Å ²)	50
Defocus range (μm)	-1.2 to -1.8
Pixel size (Å)	0.824
Symmetry imposed	C1
Initial particle images (no.)	7,124,33
Final particle images (no.)	1,099,315
Map resolution (Å)	2.57
FSC threshold	0.143
Map resolution range (Å)	2.5-3.6
Map sharpening B factor (Å ²)	-69.24
Refinement	
Initial model used (PDB code)	6NBF
Model resolution (Å)	3.1
FSC threshold	0.5
Model-Map CC (mask)	0.81
Model composition	
Non-hydrogen atoms	7893
Protein residues	1014
B factors (Å ²)	
Protein	66.78
Ligand	60.37
R.m.s. deviations	
Bond lengths (Å)	0.002
Bond angles (Å)	0.527
Validation	
MolProbity score	1.40
Clash score	7.2
Rotamer outliers (%)	0
Ramachandran plot	
Favored (%)	98
Allowed (%)	2
Disallowed (%)	0

The table contains parameters of cryo-EM data collections, data statistics, structure refinement and validation statistics of the PCO371-PTH1R-G_s complex.

Article

Extended Data Table 2 | Effects of mutations on PCO371-induced activation of PTH1R WT and mutants

Mutant	PCO371		Cell surface expression
	pEC ₅₀ ± S.E.M.	E _{max} ± S.E.M. (%WT)	(% WT)
WT	6.74 ± 0.07	100 ± 2.245	100.00 ± 1.45
R219 ^{2.46b} A	6.23 ± 0.08	100.66 ± 2.76	46.17 ± 1.96
H223 ^{2.50b} A	6.31 ± 0.09	100.30 ± 3.19	40.93 ± 0.66
L226 ^{2.53b} A	6.07 ± 0.10	101.63 ± 3.62	32.35 ± 0.99
I299 ^{3.47b} A	6.09 ± 0.12	98.02 ± 1.62	60.52 ± 0.38
E302 ^{3.50b} A	5.85 ± 0.14	102.31 ± 5.59	47.56 ± 0.63
L306 ^{3.54b} A	6.78 ± 0.06	97.62 ± 1.76	78.32 ± 1.30
K408 ^{6.40b} A	6.63 ± 0.09	99.61 ± 2.98	77.45 ± 1.02
V412 ^{6.44b} A	7.49 ± 0.12	97.29 ± 2.44	97.10 ± 2.27
L413 ^{6.45b} A	6.01 ± 0.11	102.69 ± 4.35	72.94 ± 1.34
M414 ^{6.46b} A	7.34 ± 0.14	97.30 ± 2.55	88.78 ± 0.59
P415 ^{6.47b} A	NA	NA	96.36 ± 0.75
L416 ^{6.48b} A	7.01 ± 0.06	98.75 ± 1.71	75.75 ± 2.54
F417 ^{6.49b} A	7.14 ± 0.05	97.42 ± 1.09	89.05 ± 1.82
I458 ^{7.56b} A	6.51 ± 0.07	99.67 ± 2.56	80.93 ± 1.81
Y459 ^{7.57b} A	6.38 ± 0.09	99.33 ± 3.05	94.38 ± 1.22
C462 ^{7.60b} A	6.32 ± 0.08	100.42 ± 3.12	86.41 ± 1.82
N463 ^{8.47b} A	6.63 ± 0.10	99.76 ± 3.19	103.10 ± 0.87
G464 ^{8.48b} A	7.07 ± 0.06	98.56 ± 1.65	100.36 ± 2.23
E465 ^{8.49b} A	6.76 ± 0.12	99.19 ± 3.05	90.05 ± 1.83

Effects of mutations on PCO371-induced activation of wild-type and mutant PTH1R. pEC₅₀ and E_{max} were calculated to determine the signaling efficiency and potency, respectively. The maximal response is reported as a percentage of the maximum effect at the WT. Data are mean ± s.e.m. from at least three independent experiments performed in technical triplicate. NA, not active. Expression levels of PTH1R mutants. The relative expression levels of PTH1R in AD293 cells were determined by flow cytometry (FACS) using WT as the reference. Cells were gated with a forward scatter cutoff at a gain value of 0.18% by using the blank sample as the reference value of background fluorescence signal. The left region represents the negative cell community, while the right region represents the positive cells that express the receptor.

Reporting Summary

Nature Portfolio wishes to improve the reproducibility of the work that we publish. This form provides structure for consistency and transparency in reporting. For further information on Nature Portfolio policies, see our [Editorial Policies](#) and the [Editorial Policy Checklist](#).

Statistics

For all statistical analyses, confirm that the following items are present in the figure legend, table legend, main text, or Methods section.

n/a Confirmed

- The exact sample size (n) for each experimental group/condition, given as a discrete number and unit of measurement
- A statement on whether measurements were taken from distinct samples or whether the same sample was measured repeatedly
- The statistical test(s) used AND whether they are one- or two-sided
Only common tests should be described solely by name; describe more complex techniques in the Methods section.
- A description of all covariates tested
- A description of any assumptions or corrections, such as tests of normality and adjustment for multiple comparisons
- A full description of the statistical parameters including central tendency (e.g. means) or other basic estimates (e.g. regression coefficient) AND variation (e.g. standard deviation) or associated estimates of uncertainty (e.g. confidence intervals)
- For null hypothesis testing, the test statistic (e.g. F , t , r) with confidence intervals, effect sizes, degrees of freedom and P value noted
Give P values as exact values whenever suitable.
- For Bayesian analysis, information on the choice of priors and Markov chain Monte Carlo settings
- For hierarchical and complex designs, identification of the appropriate level for tests and full reporting of outcomes
- Estimates of effect sizes (e.g. Cohen's d , Pearson's r), indicating how they were calculated

Our web collection on [statistics for biologists](#) contains articles on many of the points above.

Software and code

Policy information about [availability of computer code](#)

Data collection	Cryo-EM data were automatically collected using EPU 2.13 on a Titan Krios G4 at 300KV accelerating voltage equipped with Gatan K3 direct electron detector.
Data analysis	The following softwares were used in this study: CryoSPARC-v3.3.1, CTFFIND 4.1, Relion 4.0, UCSF Chimera 1.14, UCSF ChimeraX 1.3, Coot 0.9.6, Pymol 2.5.2, Phenix1.20, MODELLER (10.2), PyVOL (1.7.8), GraphPad Prism 8.0, NovoExpress Software (1.4.0), Zeiss ZEN 3.0(blue edition).

For manuscripts utilizing custom algorithms or software that are central to the research but not yet described in published literature, software must be made available to editors and reviewers. We strongly encourage code deposition in a community repository (e.g. GitHub). See the Nature Portfolio [guidelines for submitting code & software](#) for further information.

Data

Policy information about [availability of data](#)

All manuscripts must include a [data availability statement](#). This statement should provide the following information, where applicable:

- Accession codes, unique identifiers, or web links for publicly available datasets
- A description of any restrictions on data availability
- For clinical datasets or third party data, please ensure that the statement adheres to our [policy](#)

Cryo-EM map has been deposited in the Electron Microscopy Data Bank under accession code: EMD-36593 (PCO371-bound PTH1R-Gs complex). The atomic coordinate has been deposited in the Protein Data Bank under accession codes: 8J9 (PCO371-bound PTH1R-Gs complex).

Research involving human participants, their data, or biological material

Policy information about studies with [human participants or human data](#). See also policy information about [sex, gender \(identity/presentation\), and sexual orientation](#) and [race, ethnicity and racism](#).

Reporting on sex and gender

N/A

Reporting on race, ethnicity, or other socially relevant groupings

N/A

Population characteristics

N/A

Recruitment

N/A

Ethics oversight

N/A

Note that full information on the approval of the study protocol must also be provided in the manuscript.

Field-specific reporting

Please select the one below that is the best fit for your research. If you are not sure, read the appropriate sections before making your selection.

Life sciences

Behavioural & social sciences

Ecological, evolutionary & environmental sciences

For a reference copy of the document with all sections, see nature.com/documents/nr-reporting-summary-flat.pdf

Life sciences study design

All studies must disclose on these points even when the disclosure is negative.

Sample size

For cryo-EM data, images were collected until the resolution and 3D reconstruction converges. For all the functional assay, no statistical approaches were used to predetermine the sample size. We performed at least three independent experiments to ensure each data point was repeatable, commonly exploited by researcher in this field.

Data exclusions

No data were systematically excluded from the analysis.

Replication

For all functional assays, each experiment was repeated independently at least three times and each of which was performed successfully in triplicate.

Randomization

Randomization is not relevant to this study, as protein samples are not required to be divided into experimental groups in the structural studies, and no animals or human research participants are involved in this study.

Blinding

Blinding is not relevant to this study, since all the data were collected automatically.

Reporting for specific materials, systems and methods

We require information from authors about some types of materials, experimental systems and methods used in many studies. Here, indicate whether each material, system or method listed is relevant to your study. If you are not sure if a list item applies to your research, read the appropriate section before selecting a response.

Materials & experimental systems

- | | |
|-------------------------------------|---|
| n/a | Involved in the study |
| <input type="checkbox"/> | <input checked="" type="checkbox"/> Antibodies |
| <input type="checkbox"/> | <input checked="" type="checkbox"/> Eukaryotic cell lines |
| <input checked="" type="checkbox"/> | <input type="checkbox"/> Palaeontology and archaeology |
| <input checked="" type="checkbox"/> | <input type="checkbox"/> Animals and other organisms |
| <input checked="" type="checkbox"/> | <input type="checkbox"/> Clinical data |
| <input checked="" type="checkbox"/> | <input type="checkbox"/> Dual use research of concern |
| <input checked="" type="checkbox"/> | <input type="checkbox"/> Plants |

Methods

- | | |
|-------------------------------------|--|
| n/a | Involved in the study |
| <input checked="" type="checkbox"/> | <input type="checkbox"/> ChIP-seq |
| <input type="checkbox"/> | <input checked="" type="checkbox"/> Flow cytometry |
| <input checked="" type="checkbox"/> | <input type="checkbox"/> MRI-based neuroimaging |

Antibodies

Antibodies used

Antibody used: The primary antibody was the mouse Anti-DDDDK-Tag mAb (abclonal, Cat# AE005) and was used in 1:100 dilution. The secondary antibody was Alexa FluorTM 488 goat anti-mouse IgG (H+L) (Invitrogen, Cat #A11029) and was used in 1:1000 dilution.

Validation

All antibodies used are commercially purchased and have been validated by the vendors. All antibodies are well characterized and were applied according to data sheet information
 Mouse Anti-DDDDK-Tag mAb: <https://abclonal.com.cn/catalog/AE005>;
 secondary anti-mouse antibody: <https://www.thermofisher.com/cn/zh/antibody/product/Goat-anti-Mouse-IgG-H-L-CrossAdsorbed-Secondary-Antibody-Polyclonal/A-11029>;

Eukaryotic cell lines

Policy information about [cell lines](#) and [Sex and Gender in Research](#)

Cell line source(s)

Sf9 (Invitrogen), AD293 cells (Agilent);HEK-293 cells(ATCC)

Authentication

All of the cell lines are maintained by the supplier. No additional authentication was performed by the authors of this study.

Mycoplasma contamination

Cell lines were tested and free from mycoplasma contamination.

Commonly misidentified lines (See [ICLAC](#) register)

No commonly misidentified cell lines were used.

Flow Cytometry

Plots

Confirm that:

- The axis labels state the marker and fluorochrome used (e.g. CD4-FITC).
- The axis scales are clearly visible. Include numbers along axes only for bottom left plot of group (a 'group' is an analysis of identical markers).
- All plots are contour plots with outliers or pseudocolor plots.
- A numerical value for number of cells or percentage (with statistics) is provided.

Methodology

Sample preparation

AD293 cells were collected after 24 hours of transient transfection and then blocked with 5% BSA in PBS at RT for 15 min followed by incubation with primary mouse anti-Flag antibody (1:100) at RT for 1 hour. The cells were then washed three times with PBS containing 1% BSA and incubated with anti-mouse Alexa-488-conjugated secondary antibody (1:1000) at 4 °C in the dark for 1h. After another three washes, the cells were resuspended with 500 µl PBS containing 1% BSA for detection in ACEA NovoCyte 3000 flow cytometer system (Angilent Biosciences) at excitation 488 nm and emission 530 nm. For each sample, approximately 8000 cellular events were collected.

Instrument

ACEA NovoCyte 3000 flow cytometer system (Angilent Biosciences)

Software

NovoExpress Software (1.4.0), GraphPad Prism 8.0

Cell population abundance

Approximately 8,000 cellular events were collected and the total fluorescence intensity of positive expression cell population was calculated.

Gating strategy

The cells were gated with a forward scatter cutoff at a gain value of 0.18% by using the blank sample as the reference value of background fluorescence signal. The left region represents the negative cells, while the right region represents the positive cells that express the receptor.

Tick this box to confirm that a figure exemplifying the gating strategy is provided in the Supplementary Information.